J. Fluid Mech. (1994), *vol.* 279, *pp.* 377–405

Nonlinear resonance of free surface waves in a current over a sinusoidal bottom: a numerical study

By PAOLO SAMMARCO, CHIANG C. MEI AND KARSTEN TRULSEN

Department of Civil and Environmental Engineering, Massachusetts Institute of Technology, Cambridge, MA 02139, USA

(Received 18 February 1994 and in revised form 23 June 1994)

We examine the free surface flow over a fixed bed covered by rigid sinusoidal dunes. The mean current velocity is near the critical value at which the linearized theory predicts unbounded response. By allowing transients we examine the instability of the steady and nonlinear solution of Mei (1969) and the possibility of chaos when the current has a small oscillatory component.

1. Introduction

The problem of dune formation and migration on a river bed has long fascinated hydraulicians. Scientific efforts in the last thirty years owe much to the seminal work of Kennedy (1963) who studied the instability of long-crested sand dunes under various regimes of steady flow. Assuming potential flow in the running stream he accounted for the sediment motion by an empirical transport rate formula, with an additional hypothesis of a phase shift between the sediment transport rate and the propagation speed of the sand dunes. Since the sand dunes evolve very slowly in time, the bed was treated as being fixed and the flow above steady. Specifically for a sinusoidal bed

$$B = b\cos kx \tag{1.1}$$

over a mean depth h, with $b/h \ll 1$, the linearized potential theory gives the following free surface displacement:

$$\zeta = \frac{kb\cos kx}{k\cosh kh - (g/U^2)\sinh kh} \tag{1.2}$$

(Lamb 1932). There is a critical velocity U_0 defined by the zero of the denominator in the preceding equation:

$$U_0^2 = \frac{g}{k}\tanh kh. \tag{1.3}$$

When the flow is subcritical, i.e. $U < U_0$, the free surface and the bed waves are opposite in phase, the corresponding bed waves are called dunes. On the other hand, when the flow is supercritical, i.e. $U > U_0$, the free surface and the bed waves are in phase, the bed waves are called the antidunes. When $U = U_0$, however, the surface wave becomes unbounded for a prescribed bed wave amplitude. To avoid unbounded response, Lamb (1932) suggested that viscous damping should be

introduced. Kennedy (1963) suggested that, since the free surface amplitude cannot be infinite, either the sand dune amplitude must diminish to zero, as is often observed in the regime of critical flow, or else the flow must not remain steady for fixed dunes.

Unboundedness in the linear theory of course implies resonance. Indeed U_0 is precisely the phase velocity of a free surface wave of wavenumber k over a horizontal bottom. In the coordinate system moving with the current, the bed is a sinusoidal progressive wave advancing at the speed U. Clearly if U is equal or close to the phase velocity of a free surface wave of the same wavenumber, resonance is expected. To remove the unphysical singularity, Mei (1969) resorted to nonlinearity and modified the Stokes wave theory for a horizontal bottom to one for a rigid sinusoidal bottom. The free surface was taken to be steady relative to the wavy bed. For certain range of U near U_0, the free surface wave amplitude can be triple-valued; the relation between the equilibrium amplitude and the velocity departure from resonance is cubic, as in the Duffing problem in nonlinear oscillators. An instability analysis is needed to decide which of the triple roots is likely to occur in nature; this was however not carried out by Mei. A similar steady-state analysis has been reported recently by Zhu (1992) for a uniform flow in a horizontal channel of rectangular cross-section with sinusoidally varying sidewalls. The related instability problem for a stationary interfacial wave over a fixed wavy bed has now been studied by Miles (1986). By adding a simple dissipation term in the transient evolution equation he found Hopf bifurcations which give rise to limit cycles and period doublings. Bontozoglou, Kalliadasis & Karabelas (1991) have recently reported exact numerical solutions to the fully nonlinear potential theory of steady free surface flows over a wavy bed. For sufficiently small wave steepness, their numerical computation of the synchronous resonance branches is shown to agree with the undamped limit of the weakly nonlinear theory of Miles. By parametrically varying the current speed U, the authors have also given numerical evidence of subharmonic resonances, where the surface wave is one half and one third as long as the bed wave.

In this paper we shall extend the earlier works on surface waves on a current over a wavy bed. In particular, we shall examine the initial stability and the long-time evolution of weakly nonlinear waves resonated by the bed. The dunes are assumed to be rigid, of uniform amplitude, and infinite in numbers, extending to infinities in both upstream and downstream directions. As usual in weak resonance theories, the waves are expected to be modulated slowly. The slow evolution equation for the complex amplitude of the surface wave is deduced by first allowing modulations in both time and space. Analytical and numerical studies are limited to the simpler case of time modulation, so that the dynamical system involves only ordinary differential equations. For a steady current the dynamical system is autonomous and reducible to that governing the Duffing oscillators (Jordan & Smith 1986), or the resonant bubble response induced by oscillating sound pressure (Hall & Seminara 1980).

Principal attention will be directed to the effect of a small oscillatory component in the incident current. The evolution equation is then changed to a non-autonomous dynamical system of the second order; chaos is now possible. Mathematically our problem is ultimately reduced to a Duffing problem with periodic forcing and coefficients (see e.g. Yagasaki, Sakata & Kimura 1990). Our objectives here are to examine numerically the development of chaos as a function of the physical parameters and its physical implications. Both synchronous and subharmonic resonances will be

discussed here. Dissipation by viscosity, as well as slow modulations in space, both of which can be important in nature, are left for future studies.

2. Derivation of evolution equations by multiple-scales analysis

We consider a nearly horizontal river bed described by $z = -h + B(x)$ where h is the constant mean depth and $B(x)$ the dune height above the mean bottom. Let U be the velocity of a uniform current in the absence of dunes and $\boldsymbol{u}$ be the disturbance velocity due to the dunes. The flow is assumed to be irrotational so that the total potential Φ and the disturbance potential ϕ are related by

$$\Phi(x,z,t) = Ux + \phi(x,z,t), \tag{2.1}$$

and $\boldsymbol{u} = \nabla\phi$. The disturbance potential is governed by

$$\phi_{xx} + \phi_{zz} = 0. \tag{2.2}$$

On the free surface, $z = \zeta(x,t)$, the dynamic boundary condition is just the Bernoulli equation:

$$g\zeta + \phi_t + U\phi_x + \tfrac{1}{2}|\boldsymbol{u}|^2 = 0, \qquad z = \zeta(x,t); \tag{2.3}$$

while the kinematic and dynamic boundary conditions can be combined to give

$$\phi_{tt} + g\phi_z + \boldsymbol{u}_t^2 + \tfrac{1}{2}\boldsymbol{u}\cdot\nabla\boldsymbol{u}^2 + U^2\phi_{xx} + 2U\phi_{xt} + U\boldsymbol{u}_x^2 = 0, \qquad z = \zeta(x,t), \tag{2.4}$$

where on the bottom $z = -h + B$ the kinematic boundary condition requires

$$\phi_z = B_x(U + \phi_x). \tag{2.5}$$

We now extend Mei (1969) by allowing unsteadiness in addition to nonlinearity.

We shall assume both $\zeta = O(A)$ and $B = O(b)$ to be small compared to $1/k$. Taylor expansion of the free surface boundary conditions (2.3) and (2.4) gives respectively

$$g\zeta + \phi_t + U\phi_x + \tfrac{1}{2}|\boldsymbol{u}|^2 + \zeta(\phi_{tz} + U\phi_{xz} + \phi_x\phi_{xz} + \phi_z\phi_{zz}) + \tfrac{1}{2}\zeta^2(\phi_{tzz} + U\phi_{xzz}) + \cdots = 0 \tag{2.6}$$

and

$$\begin{aligned}\phi_{tt} + g\phi_z + U^2\phi_{xx} + 2U\phi_{xt} + U\boldsymbol{u}_x^2 + \boldsymbol{u}_t^2 \\ + \zeta\left(\phi_{ttz} + g\phi_{zz} + U^2\phi_{xxz} + 2U\phi_{xtz} + U\boldsymbol{u}_{xz}^2 + \boldsymbol{u}_{tz}^2\right) + \tfrac{1}{2}\boldsymbol{u}\cdot\nabla\boldsymbol{u}^2 \\ + \tfrac{1}{2}\zeta^2\left(\phi_{ttzz} + g\phi_{zzz} + U^2\phi_{xxzz} + 2U\phi_{xtzz} + U\boldsymbol{u}_{xzz}^2 + \boldsymbol{u}_{tzz}^2\right) + \cdots = 0.\end{aligned} \tag{2.7}$$

Similarly, Taylor expansion of the kinematic boundary condition about $z = -h$ gives

$$\phi_z + B\phi_{zz} + \tfrac{1}{2}B^2\phi_{zzz} + \cdots = B_x(U + \phi_x + B\phi_{xz} + \tfrac{1}{2}B^2\phi_{xzz} + \cdots). \tag{2.8}$$

We now introduce the small parameter $\epsilon = kA \ll 1$ which represents the small wave steepness, and assume $kb \ll 1$ to be no greater than $O(\epsilon)$. As our attention will be focussed on the neighbourhood of resonance, slow growth in time is expected. For generality, we introduce slow coordinates in both time and space as follows:

$$\begin{aligned} &x, && x_1 = \epsilon x, && x_2 = \epsilon^2 x, \ \ldots, \\ & && t_1 = \epsilon t, && t_2 = \epsilon^2 t, \ \ldots. \end{aligned}$$

Let us assume multiple-scale expansions for both ϕ and ζ:

$$\phi = \sum_{n=1} \epsilon^n \phi_n(x, x_1, x_2, \ldots; z; t_1, t_2, \ldots), \tag{2.9}$$

$$\zeta = \sum_{n=1} \epsilon^n \zeta_n(x, x_1, x_2, \ldots; t_1, t_2, \ldots), \tag{2.10}$$

and allow the incident current velocity U to be slightly detuned from resonance:

$$U = U_0 + \epsilon U_1 + \epsilon^2 U_2 + \ldots. \tag{2.11}$$

We also expand B as follows:

$$B = \sum_{n=1} \epsilon^n B_n(x, x_1, x_2 \ldots). \tag{2.12}$$

Substituting expansions (2.9), (2.10), (2.11), (2.12) into (2.2) and (2.6), (2.7), (2.8), and following the standard procedure, we obtain a sequence of perturbation equations. Only the results from the bottom boundary condition are recorded below:

$$\phi_{1_z} = U_0 B_{1_x}, \tag{2.13}$$

$$\phi_{2_z} = U_0(B_{2_x} + B_{1_{x_1}}) + B_{1_x}(U_1 + \phi_{1_x}) - B_1 \phi_{1_{zz}}, \tag{2.14}$$

$$\begin{aligned}\phi_{3_z} = {} & U_0(B_{3_x} + B_{2_{x_1}} + B_{1_{x_2}}) + B_{2_x}(U_1 + \phi_{1_x}) + U_1 B_{1_{x_1}} \\ & + B_{1_x}(U_2 + \phi_{2_x} + \phi_{1_{x_1}} + B_1 \phi_{1_{xz}}) - (B_1 \phi_{2_{zz}} + B_2 \phi_{1_{zz}} + \tfrac{1}{2} B_1^2 \phi_{1_{zzz}}).\end{aligned} \tag{2.15}$$

We shall consider resonances resulting in a free surface wave proportional to $\epsilon \exp(\pm ikx)$ at $O(\epsilon)$ and a uniformly valid theory involving terms no higher than $O(\epsilon^3)$. It will now be shown that through quadratic and cubic nonlinearities, resonance can be accomplished by a sinusoidal bottom proportional to any one of the harmonics:

$$e^{\pm ipkx}, \quad p = \left(\tfrac{1}{3}, \tfrac{1}{2}, 1, 2, 3\right). \tag{2.16}$$

The corresponding resonance will be called *synchronous* if $p = 1$, *superharmonic* if $p = \frac{1}{3}, \frac{1}{2}$, and *subharmonic* if $p = 2, 3$.

We consider the interaction between the free surface wave of displacement

$$\tfrac{1}{2}(Ae^{ikx} + *) \tag{2.17}$$

and bed waves of different magnitudes and harmonics, with a view to obtaining the evolution equation for A from the solvability conditions for $\epsilon A e^{ikx} + *$; the $*$ indicates the conjugate quantity. For each case, we itemize below the type of resonance in (*a*), and the bed wave form in (*b*). The terms arising from quadratic nonlinearity are listed in (*c*). The coefficients of the first harmonic e^{ikx} of all $O(\epsilon^3)$ terms due to cubic nonlinearity are then given in (*d*). From the solvability condition, the expected final evolution equation for A is of the following general type

$$\frac{\partial A}{\partial t_2} + \alpha \frac{\partial A}{\partial x_2} + \beta A + \gamma |A|^2 A = F(A, b). \tag{2.18}$$

The right-hand side F will be listed in (*e*).

Case 1:

(*a*) Synchronous resonance ($p = 1$),

(*b*) $\epsilon^3 (be^{ikx} + *)$,

(*c*) $\epsilon^2 (|A|^2, A^2 e^{2ikx} + *)$,

(*d*) $\epsilon^3 \left((|A|^2 A, b, A, \partial A/\partial t_2, \partial A/\partial x_2) e^{ikx} + *\right)$,

(*e*) δb.

Case 2:

(*a*) Subharmonic resonance ($p = 2$),

(*b*) $\epsilon^2 \left(b\,\mathrm{e}^{2ikx} + *\right)$,

(*c*) $\epsilon^2 \left(|A|^2,\ A^2\mathrm{e}^{2ikx} + *\right),\quad \epsilon^3 \left(b\,A^*\mathrm{e}^{ikx} + *\right)$,

(*d*) $\epsilon^3 \left(\left(|A|^2A, A, \partial A/\partial t_2, \partial A/\partial x_2\right)\mathrm{e}^{ikx} + *\right)$,

(*e*) $\delta A^* b$.

Case 3:

(*a*) Subharmonic resonance ($p = 3$),

(*b*) $\epsilon \left(\mathrm{e}^{3ikx} + *\right)$,

(*c*) $\epsilon^2 \left(|A|^2,\ |b|^2,\ A^2\,\mathrm{e}^{2ikx},\ b^2\,\mathrm{e}^{6ikx},\ bA^*\,e^{2ikx} + *\right), \epsilon^3 \left(b\,A^{*2}\,e^{ikx} + *\right)$,

(*d*) $\epsilon^3 \left(\left(|A|^2\,A,\ A,\ \partial A/\partial t_2, \partial A/\partial x_2,\ |b|^2\,A,\ A^{*2}b\right)\mathrm{e}^{ikx} + *\right)$,

(*e*) $\delta A^{*2}b + \chi A|b|^2$.

Case 4:

(*a*) Superharmonic resonance $\left(p = \frac{1}{2}\right)$,

(*b*) $\epsilon^{3/2} \left(b\,\mathrm{e}^{ikx/2} + *\right)$,

(*c*) $\epsilon^2 \left(|A|^2,\ A^2\,\mathrm{e}^{2ikx} + *\right), \epsilon^{5/2} \left(A\,b\,\mathrm{e}^{3ikx/2}, A\,b^*\mathrm{e}^{ikx/2} + *\right), \epsilon^3 \left(b^2\mathrm{e}^{ikx} + *\right)$,

(*d*) $\epsilon^3 \left(\left(|A|^2A,\ A|b|^2,\ b^2,\ A, \partial A/\partial t_2,\ \partial A/\partial x_2\right)\mathrm{e}^{ikx} + *\right)$,

(*e*) $\delta A|b|^2 + \chi b^2$.

Case 5:

(*a*) Superharmonic resonance $\left(p = \frac{1}{3}\right)$,

(*b*) $\epsilon \left(b\,\mathrm{e}^{ikx/3} + *\right)$,

(*c*) $\epsilon^2 \left(|A|^2, |b|^2,\ A^2\,\mathrm{e}^{2ikx},\ b^2\,\mathrm{e}^{2ikx/3},\ A\,b\,\mathrm{e}^{4ikx/3},\ A\,b^*\,\mathrm{e}^{2ikx/3} + *\right)$,

(*d*) $\epsilon^3 \left(\left(|A|^2A,\ A,\ |b|^2A,\ b^3,\ \partial A/\partial t_2,\ \partial A/\partial x_2\right)\mathrm{e}^{ikx} + *\right)$,

(*e*) $\delta A|b|^2 + \chi b^3$.

In summary, the evolution equations are of the cubic Schrödinger type with additional terms involving the bed wave amplitude. We note that the two superharmonic cases are similar in form to the synchronous case as far as A is concerned. Hence the dynamics are mathematically similar. In this paper, we shall examine the synchronous and the ($p = 2$) subharmonic cases in detail. With the nth-order terms expanded into harmonics as follows:

$$\left.\begin{aligned} \phi_n &= \sum_{m=-n}^{n} \mathrm{e}^{imkx}\phi_{nm}(x, x_1, x_2, \ldots; z; t_1, t_2, \ldots), \\ \zeta_n &= \sum_{m=-n}^{n} \mathrm{e}^{imkx}\zeta_{nm}(x, x_1, x_2, \ldots; z; t_1, t_2, \ldots), \end{aligned}\right\} \tag{2.19}$$

we find that, at the nth order, the mth harmonic ϕ_{nm} is governed by a boundary value problem in the vertical coordinate z. The first-harmonic problem is homogeneous at the first order but inhomogeneous at higher orders. Invoking solvability at the second and third orders yields the evolution equations for the amplitude of the homogeneous solution. The procedure is standard, as illustrated in Mei (1989) for a horizontal bottom. Therefore only the key results are presented here.

Thus far the different resonant wavenumbers of the dunes have been identified for the same the free surface wavelength, hence the same resonant current speed U_0. Conversely, for a fixed dune length $2\pi/K$, the resonant current speed is found from

$$U_0^2 = p\frac{g}{K}\tanh\frac{Kh}{p}, \qquad p = \left(\tfrac{1}{3}, \tfrac{1}{2}, 1, 2, 3\right),$$

while the corresponding wavenumber of the resonant free surface wave is K/p. Thus for larger p, the resonant current speed is higher and the free surface wave is longer.

2.1. *Synchronous resonance*

Synchronous resonance can be excited by a sinusoidal bottom two orders of magnitude smaller than the free surface:

$$B = \epsilon^3 B_3 = \epsilon^3(\tfrac{1}{2} b\, e^{ikx} + *) \quad \text{with } b = b(x_1, x_2, \ldots); \quad B_1 = B_2 = 0. \tag{2.20}$$

Let the current be

$$U = U_0 + \epsilon^2 U_2(t_2), \tag{2.21}$$

where U_0 is the constant critical speed and U_2 is the prescribed detuning from resonance at $O(\epsilon^2)$. The first-order solution is then

$$\phi_1 = \phi_{10}(x_1, x_2, \ldots; t_1, t_2, \ldots) + \frac{igA}{2kU_0} \frac{\cosh k(z+h)}{\cosh kh} e^{ikx} + *, \tag{2.22}$$

and

$$\zeta_1 = \tfrac{1}{2} A e^{ikx} + *, \tag{2.23}$$

where the free surface amplitude is a function of the slow variables $A = A(x_1, x_2, \ldots; t_1, t_2, \ldots)$. At the second order, solvability for the first harmonic gives

$$A_{t_1} + U_0(1-n)A_{x_1} = 0, \tag{2.24}$$

where

$$n = \frac{1}{2}\left(1 + \frac{2kh}{\sinh 2kh}\right) \tag{2.25}$$

is the ratio of group velocity to phase velocity for a progressive wave in non-flowing water of constant depth h. At the third order the *zeroth* harmonic must be subject to a solvability constraint:

$$\begin{aligned} &\phi_{10_{t_1 t_1}} + 2U_0 \phi_{10_{x_1 t_1}} + (U_0^2 - gh)\phi_{10_{x_1 x_1}} \\ &\quad + \frac{gkU_0}{4}\left(3\coth kh - \frac{kh}{\cosh^2 kh}\right)|A|^2_{x_1} + \frac{gk}{2\tanh kh}|A|^2_{t_1} = 0 \end{aligned} \tag{2.26}$$

which describes a long wave induced by the slow variation of the free surface amplitude. At the same order $O(\epsilon^3)$, the solvability condition for the first harmonic gives

$$\begin{aligned} iA_{t_2} + iU_0(1-n)A_{x_2} = &-\frac{U_0}{2k}\left[1 + \frac{2kh(\sinh^2 kh - 1)}{\sinh 2kh}\right] A_{x_1 t_1} - \frac{1 + kh\tanh kh}{k} A_{x_1 t_1} \\ &- \frac{1}{2U_0} A_{t_1 t_1} + k\left[U_2 + \frac{\phi_{10_{t_1}} + U_0 \phi_{10_{x_1}}}{2U_0 \cosh^2 kh} + \phi_{10_{t_1}}\right] A \\ &- \frac{k^3 U_0}{16}\left[\frac{2}{\cosh^2 kh} + \frac{3(1 + 2\cosh^2 kh)}{\sinh^4 kh} + 8\right]|A|^2 A - \frac{kU_0}{2\cosh kh} b. \end{aligned} \tag{2.27}$$

Equations (2.26) and (2.27) form a system which couples the evolutions of ϕ_{10} and A. Since from (2.24),

$$A_{t_1 t_1} = U_0^2(1-n)^2 A_{x_1 x_1}, \quad A_{x_1 t_1} = -U_0(1-n)A_{x_1 x_1}, \tag{2.28}$$

(2.27) may be rewritten

$$\begin{aligned} \mathrm{i}A_{t_2} + \mathrm{i}U_0(1-n)A_{x_2} = &-\frac{U_0}{2k}\left(n^2 + \frac{k^2h^2}{\cosh^2 kh} - \frac{2kh}{\sinh 2kh}\right)A_{x_1x_1} \\ &+ k\left[U_2 + \frac{\phi_{10_{t_1}} + U_0\phi_{10_{x_1}}}{2U_0\cosh^2 kh} + \phi_{10_{t_1}}\right]A \\ &- \frac{k^3U_0}{16}\left[\frac{2}{\cosh^2 kh} + \frac{3(1+2\cosh^2 kh)}{\sinh^4 kh} + 8\right]|A|^2A - \frac{kU_0}{2\cosh kh}b. \end{aligned} \tag{2.29}$$

Equations (2.26) and (2.29) may be used to study the slow evolution over a large but finite number of bars when the incident current is slowly varying in time. In the limit of no modulation, i.e. strict uniformity in time and space, (2.29) reduces to that of Mei (1969). Note that the last term represents forcing of the surface wave by the dunes.

In this paper we shall restrict ourselves to infinitely many dunes of spatially uniform amplitude, i.e. b is independent of x_1 and x_2. It will also be assumed that there is no spatial modulation in A with respect to coordinates x_1, x_2. It then follows from (2.24) that $A_{t_1} = 0$. From (2.26) ϕ_{10} is then decoupled from A, hence $\phi_{10_{t_1}}$ is at most a constant and may be absorbed by U_2 without loss of generality. Thus the evolution equation (2.29) is simplified to an inhomogeneous Stuart–Landau equation:

$$\mathrm{i}A_{t_2} = kU_2A - \frac{k^3U_0}{16}\left[\frac{2}{\cosh^2 kh} + \frac{3(1+2\cosh^2 kh)}{\sinh^4 kh} + 8\right]|A|^2A - \frac{kU_0}{2\cosh kh}b, \tag{2.30}$$

which is of the form anticipated in (2.19) and will be analysed later in § 3 and 4.

2.2. *1/2 subharmonic resonance*

Here we assume

$$B = \epsilon^2 B_2 = \epsilon^2(\tfrac{1}{2}b\,e^{2kx} + *) \quad \text{with} \quad b = b(x_1, x_2, \ldots); \quad B_1 = B_3 = 0. \tag{2.31}$$

The first-order solution (2.22), (2.23), as well as the solvability conditions for ϕ_{21} and ϕ_{30} (2.24) and (2.26) still hold. Consequently (2.28) remains true. At $O(\epsilon^3)$, the solvability condition for ϕ_{31} can be rearranged, by making use of (2.28), to yield the following evolution equation:

$$\begin{aligned} \mathrm{i}A_{t_2} + U_0(1-n)A_{x_2} = &-\frac{U_0}{2k}\left(n^2 + \frac{k^2h^2}{\cosh^2 kh} - \frac{2kh}{\sinh 2kh}\right)A_{x_1x_1} \\ &+ k\left[U_2 + \frac{\phi_{10_{t_1}} + U_0\phi_{10_{x_1}}}{2U_0\cosh^2 kh} + \phi_{10_{t_1}}\right]A \\ &- \frac{k^3U_0}{16}\left[\frac{2}{\cosh^2 kh} + \frac{3(1+2\cosh^2 kh)}{\sinh^4 kh} + 8\right]|A|^2A \\ &- k^2U_0\left[\sinh 2kh - \frac{1}{2\sinh 2kh} + \frac{1}{4}\left(1 - 2\sinh^2 kh\right)\left(\tanh kh + \frac{3}{\tanh^2 kh}\right)\right]A^*b, \end{aligned} \tag{2.32}$$

which differs from (2.29) in the last term proportional to b.

Again for strictly constant dune amplitude there is no spatial modulation and the above evolution equation reduces to the following Stuart–Landau equation:

$$iA_{t_2} = kU_2A - \frac{k^3U_0}{16}\left[\frac{2}{\cosh^2kh} + \frac{3(1+2\cosh^2kh)}{\sinh^4kh} + 8\right]|A|^2A$$
$$- k^2U_0\left[\sinh 2kh + \frac{1}{2\sinh 2kh} + \frac{1}{4}(1-2\sinh^2kh)(\tanh kh + \frac{3}{\tanh^2kh})\right]A^*b \quad (2.33)$$

as expected for Case 2. A similar evolution equation has been deduced before by Hall & Seminara (1980) for the subharmonic resonance of a bubble in an acoustic field. In their case all coefficients are constants and the equation has been solved analytically.

Although the mathematical results for the autonomous case of constant U_2 are in principle known, we shall recount the key results in order to bring out the physical implications of various bifurcations and to provide background for studying the non-autonomous case.

3. Steady incident current

3.1. *Synchronous resonance*

For constant U_2, equation (2.30) can be non-dimensionalized as follows:

$$b' = kb, \quad (3.1)$$

$$A' = \frac{1}{2}\left\{\frac{\cosh kh}{b'}\left[\frac{2}{\cosh^2kh} + \frac{3(1+2\cosh^2kh)}{\sinh^4kh} + 8\right]\right\}^{1/3} kA, \quad (3.2)$$

$$T = \left\{\frac{b'^2}{4\cosh^2kh}\left[\frac{2}{\cosh^2kh} + \frac{3(1+2\cosh^2kh)}{\sinh^4kh} + 8\right]\right\}^{1/3} kU_0t_2 \quad (3.3)$$

By separating the real and imaginary parts: $A' = X + iY$, we obtain a second-order autonomous dynamical system:

$$X_T = \sigma Y - (X^2 + Y^2)Y, \quad (3.4)$$
$$Y_T = -\sigma X + (X^2 + Y^2)X + 1, \quad (3.5)$$

where

$$\sigma = \left\{\frac{b'^2}{4\cosh^2kh}\left[\frac{2}{\cosh^2kh} + \frac{3(1+2\cosh^2kh)}{\sinh^4kh} + 8\right]\right\}^{-1/3} \frac{U_2}{U_0} \quad (3.6)$$

is the bifurcation parameter representing the velocity detuning.

This dynamical system has the integrable Hamiltonian

$$H(X,Y) = \tfrac{1}{2}\sigma(X^2+Y^2) - \tfrac{1}{4}(X^2+Y^2)^2 - X \quad (3.7)$$

which also arises in other nonlinear problems such as Duffing's oscillator (Jordan & Smith 1986). We merely recall that the fixed points X_*, Y_* of (3.4), (3.5) are given by the solutions of

$$Y_* = 0, \quad -\sigma X_* + X_*^3 + 1 = 0. \quad (3.8)$$

In general there are three fixed points which correspond to the intersections of the two curves $Z_1 = -\sigma X + X^3$ and $Z_2 = -1$ in the plane of Z versus X. There are three solutions if $\sigma > 3/4^{1/3} = 1.89$, one if $\sigma < 3/4^{1/3}$ and two if $\sigma = 3/4^{1/3}$. This is shown in figure 1, where Z_1 is plotted for two values of σ, 2.5 and -1. The Jacobian of the

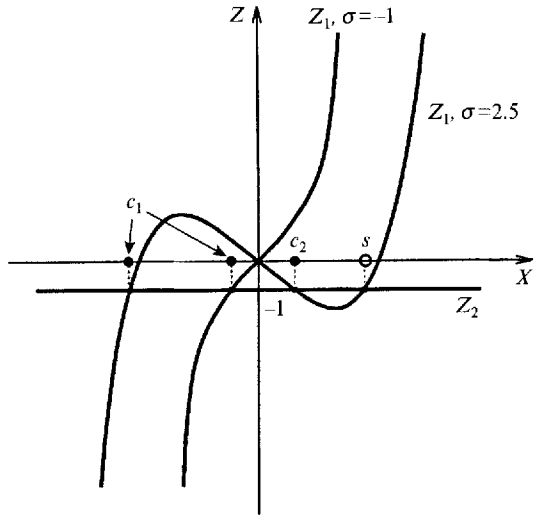

FIGURE 1. Graphical determination of the fixed points of system (3.4) and (3.5). Filled circles denote the stable fixed points, and the open circle the unstable fixed point.

system (3.4) and (3.5) at the fixed points is

$$\boldsymbol{J} = \begin{bmatrix} 0 & \sigma - X_*^2 \\ -\sigma + 3X_*^2 & 0 \end{bmatrix} = \begin{bmatrix} 0 & -\dfrac{Z_{1*}}{X_*} \\ \left.\dfrac{\mathrm{d}Z_1}{\mathrm{d}X}\right|_{X=X_*} & 0 \end{bmatrix}.$$

The eigenvalues are

$$\lambda_{1,2} = \pm \left(\frac{1}{X_*} \left.\frac{\mathrm{d}Z_1}{\mathrm{d}X}\right|_{X=X_*} \right)^{1/2}. \tag{3.9}$$

By examining $\mathrm{d}Z_1/\mathrm{d}X$ at the intersections in figure 1, we deduce that if $\sigma > 3/4^{1/3}$, two fixed points c_1 and c_2 are centres, and the third (s with the largest positive X) is a saddle, while if $\sigma < 3/4^{1/3}$ the only fixed point c_1 is a centre.

In a small neighbourhood of the centres the angular frequency Ω of the oscillation does not depend on the distance from the centre and is given by

$$\Omega \equiv \left(-\lambda_{1,2}^2\right)^{1/2} = \left(-\frac{1}{X_*} \left.\frac{\mathrm{d}Z_1}{\mathrm{d}X}\right|_{X=X_*} \right)^{1/2} = \left(\frac{\sigma - 3X_*^2(\sigma)}{X_*(\sigma)} \right)^{1/2} \tag{3.10}$$

which is a function of σ. A sample phase plane for $\sigma = 2.5$ (figure 2*a*) shows the two centres c_1 and c_2 separated by the manifolds of the saddle s (trajectories are the level curves of the Hamiltonian). Homoclinic bifurcation occurs at $\sigma = 3/4^{1/3}$: c_1 and s coalesce, as shown in the phase plane of figure 2(*b*). For a sample degenerate case of $\sigma = -1$, the phase plane with just one center is displayed in figure 2(*c*).

The bifurcation diagram is shown in figure 3.

At bifurcation we have

$$\frac{3}{4^{1/3}} = \sigma \equiv \left\{ \frac{b'^2}{4\cosh^2 kh} \left[\frac{2}{\cosh^2 kh} + \frac{3(1+2\cosh^2 kh)}{\sinh^4 kh} + 8 \right] \right\}^{-1/3} \frac{U_2}{U_0}, \tag{3.11}$$

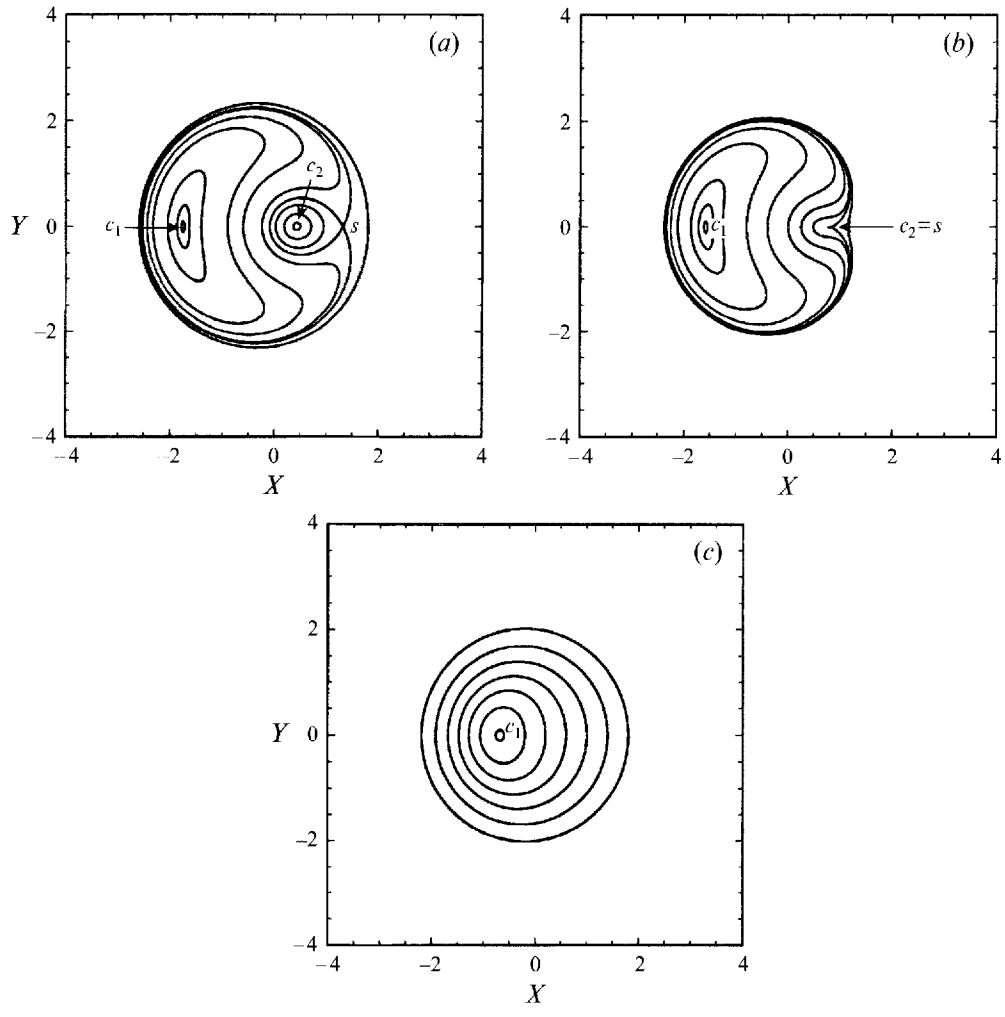

FIGURE 2. Phase-plane samples for system (3.4) and (3.5). (*a*) $\sigma = 2.5$, three fixed points; (*b*) $\sigma = 3/4^{1/3} = 1.89$ at bifurcation, one fixed point and a cusp; (*c*) $\sigma = -1$, one fixed point.

which defines a curve in the plane of $U_2 / U_0 b'^{2/3}$ *vs.* kh, displayed in figure 4: this curve separates two regions where the solution can be respectively triple- or single-valued. For very long wavelength or shallow water ($kh \ll 1$), the solution is never triple-valued near resonance, while for short wavelength or deep water ($kh \gg 1$) bifurcation happens at $U = U_0$ (i.e. $U_2 = 0$).

The physical meaning of various fixed points and phase portraits is as follows. For $\sigma > 3/4^{13}$ there are two stable steady states represented by c_1 and c_2. The state represented by c_2 corresponds to waves over antidunes; the surface wave and bed wave are in phase. The state represented by c_1 corresponds to waves over dunes; the free surface and bed waves are opposite in phase. For $\sigma < 3/4^{1/3}$ we can only have waves over dunes. Thus the line separating dunes from antidune regimes is different from the linear theory ($\sigma = 0$). Unless the initial state coincides with a fixed point, the free surface wave envelope must be periodic in time. For $\sigma > 3/4^{1/3}$, two periodic states are possible, one an antidune wave and one a dune wave; their occurrence as well as their amplitude depend on the initial conditions. Sample time series of various

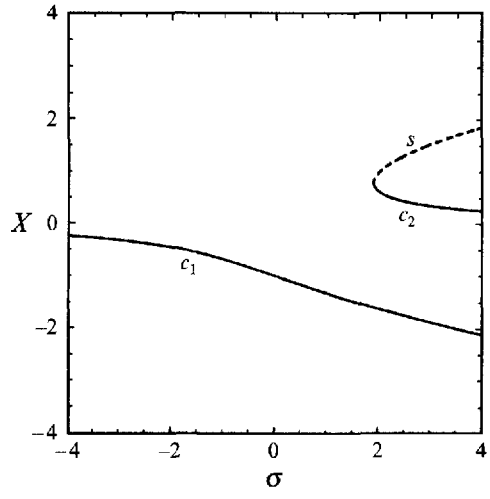

FIGURE 3. Bifurcation diagram for synchronous resonance.

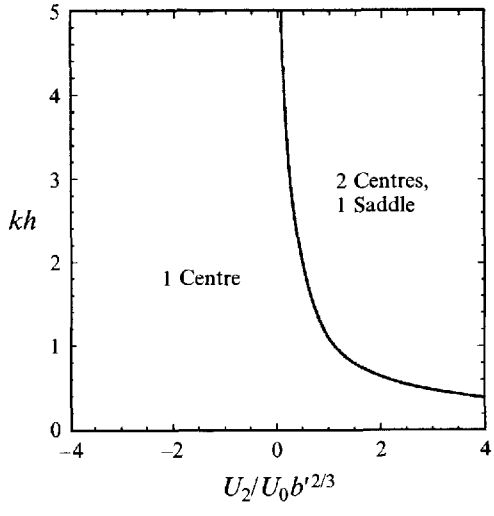

FIGURE 4. Stability diagram for synchronous resonance. Near resonance the solution is always single-valued in shallow water, and triple-valued in deep water.

orbits are shown in figure 5(*a*, *b*, *c*) for a fixed value of $\sigma = 2.5$ and various initial conditions (see also figure 2*a*). Figure 5(*a*) shows the periodic time series for an initial phase in the basin of c_2. If the initial phase point is on the manifold of the saddle, the time series has a solitary hump: the time series shown in figure 5(*b*) corresponds to the homoclinic loop around c_2. Figure 5(*c*) shows the more articulated time series for an orbit around c_1 and close to the homoclinic loops: the flat parts correspond to the portions of the orbit which are close to the saddle point.

3.2. *1/2 subharmonic resonance*

Equation (2.33) can be non-dimensionalized as follows:

$$b' = kb, \tag{3.12}$$

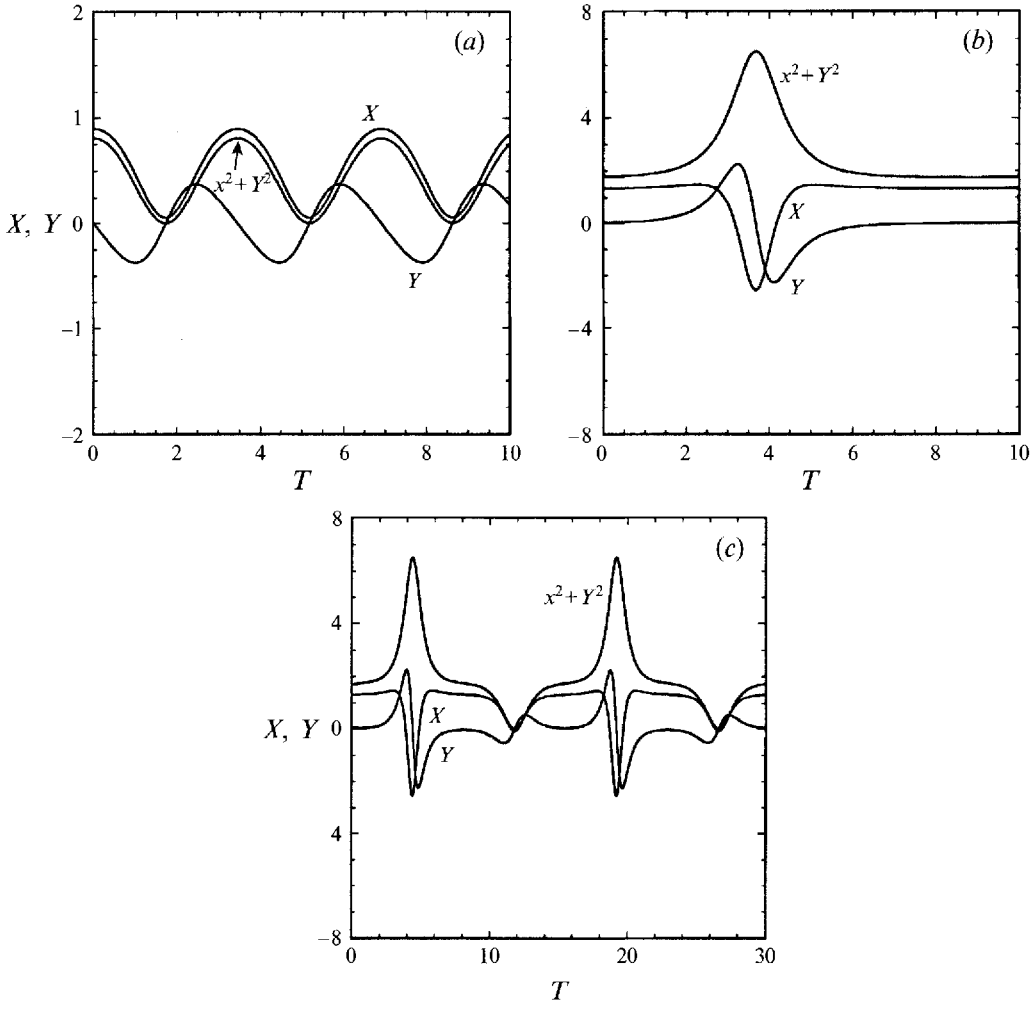

FIGURE 5. Sample time series for different initial conditions and $\sigma = 2.5$. (*a*) $X(0) = 0.9$, $Y(0) = 0$: initial phase point is in the domain of c_2; (*b*) $X(0) = 1.33$, $Y(0) \approx 0.01$, initial phase point is on the unstable manifold of the saddle s; (*c*) $X(0) = 1.3$, $Y(0) = 0.1$, initial phase point is near s; the orbit is around c_1.

$$A' = \left\{ \frac{\frac{1}{16}\left[\frac{2}{\cosh^2 kh} + \frac{3(1+2\cosh^2 kh)}{\sinh^4 kh} + 8\right]}{b'\left[\sinh 2kh - \frac{1}{2\sinh 2kh} + \frac{1}{4}(1-2\sinh^2 kh)(\tanh kh + \frac{3}{\tanh^2 kh})\right]} \right\}^{1/2} kA, \quad (3.13)$$

$$T = b'\left[\sinh 2kh - \frac{1}{2\sinh 2kh} + \frac{1}{4}(1-2\sinh^2 kh)(\tanh kh + \frac{3}{\tanh^2 kh})\right] kU_0 t_2. \quad (3.14)$$

By separating the real and imaginary parts: $A' = X + \mathrm{i}Y$, a second-order dynamical system is obtained from (2.33):

$$X_T = (1+\sigma)\,Y - (X^2 + Y^2)\,Y, \quad (3.15)$$

$$Y_T = (1-\sigma)\,X + (X^2 + Y^2)\,X. \quad (3.16)$$

In this case the bifurcation parameter σ is related to the velocity detuning by

$$\sigma = \left\{ b' \left[\sinh 2kh + \frac{1}{2\sinh 2kh} + \frac{1}{4}(1 - 2\sinh^2 kh)(\tanh kh + \frac{3}{\tanh^2 kh}) \right] \right\}^{-1} \frac{U_2}{U_0}. \tag{3.17}$$

Equations (3.14) and (3.15) constitute an integrable Hamiltonian system with

$$H(X, Y) = \tfrac{1}{2}\sigma(X^2 + Y^2) - \tfrac{1}{4}(X^2 + Y^2)^2 + \tfrac{1}{2}(Y^2 - X^2). \tag{3.18}$$

Although an implicit but exact solution is known (Hall & Seminara 1980), it is convenient to employ the phase plane analysis and examine the fixed points, defined by

$$\left.\begin{array}{lll} X_* = 0, & Y_* = 0, & \text{for all } \sigma, \\ X_* = 0, & Y_* = \pm(\sigma + 1)^{1/2}, & \sigma > -1, \\ X_* = \pm(\sigma - 1)^{1/2}, & Y_* = 0, & \sigma > 1. \end{array}\right\} \tag{3.19}$$

Thus, there are five fixed points if $\sigma > 1$, three if $\sigma \in (-1, 1)$ and one if $\sigma < -1$. Physically the first fixed point at the origin is the trivial state of flat free surface while the second pair with $X_* = 0$, c^+ and c^-, are waves whose alternating crests and troughs lie above the troughs of the bed wave. Corresponding to the last pair with $X_* = \pm(\sigma - 1)^{1/2}$ and $Y_* = 0$, s^+ and s^-, the free surface has its crests and troughs directly above the crests of the bed wave.

The Jacobian at the origin is

$$\boldsymbol{J} = \begin{bmatrix} 0 & 1 + \sigma \\ 1 - \sigma & 0 \end{bmatrix}$$

so that its eigenvalues are:

$$\lambda_{1,2} = \pm(1 - \sigma^2)^{1/2}. \tag{3.20}$$

The origin is therefore a saddle for $\sigma \in (-1, 1)$, and a centre for $\sigma \notin (-1, 1)$. In the latter case the natural angular frequency of the oscillation around the origin is given by

$$\Omega \equiv (-\lambda_{1,2}^2)^{1/2} = (\sigma^2 - 1)^{1/2}. \tag{3.21}$$

The Jacobian at the symmetric fixed points c^+ and c^- on the Y-axis is

$$\boldsymbol{J} = \begin{bmatrix} 0 & -2(1 + \sigma) \\ 2 & 0 \end{bmatrix}$$

with eigenvalues

$$\lambda_{1,2} = \pm 2\mathrm{i}(1 + \sigma)^{1/2}. \tag{3.22}$$

Since they exist only for $\sigma > -1$, c^+ and c^- are always centres, and the linearized frequency of oscillation is

$$\Omega \equiv (-\lambda_{1,2}^2)^{1/2} = 2(1 + \sigma)^{1/2}. \tag{3.23}$$

Finally for the symmetric fixed points s^+ and s^- on the X-axis, the Jacobian is

$$\boldsymbol{J} = \begin{bmatrix} 0 & 2 \\ 2\sigma & 0 \end{bmatrix}$$

and the eigenvalues are

$$\lambda_{1,2} = \pm 2\sigma^{1/2}. \tag{3.24}$$

Since s^+ and s^- exist for $\sigma > 1$, they are always saddles.

Figure 6(*a*) shows the phase plane for $\sigma = 2.0$, when all five fixed points exist: three centres on the Y- axis and two saddles on the X- axis. Two heteroclinic orbits separate the basins of three centres. When σ decreases, s^+ and s^- move towards the origin (recall that $X_* = \pm(\sigma-1)^{1/2}$) and the size of the central basin around the origin itself decreases. For $\sigma = 1$ they coalesce with the origin (homoclinic bifurcation), which then becomes unstable (saddle). The corresponding phase plane is displayed in figure 6(*b*) ($\sigma = 0$).

As σ decreases further below zero, the two centres on the Y- axis c^+ and c^- drift towards the origin ($Y_* = \pm(\sigma + 1)^{1/2}$) and eventually coalesce with the latter when $\sigma = -1$. After this second homoclinic bifurcation, the centre at the origin remains to be the only fixed point; the corresponding phase plane is shown in figure 6(*c*). The bifurcation diagram is given in figure 7, where the origin is seen to be unstable when $\sigma \in (-1, 1)$. The instability of the origin implies that small perturbations from the null solution give rise to finite-amplitude oscillations with the phase point tracing a periodic orbit around the two centres (see figure 6(*b*)).

The two homoclinic bifurcations occur when

$$\pm 1 = \sigma \equiv \left\{ b' \left[\sinh 2kh + \frac{1}{2\sinh 2kh} + \frac{1}{4}(1 - 2\sinh^2 kh)(\tanh kh + \frac{3}{\tanh^2 kh}) \right] \right\}^{-1} \frac{U_2}{U_0} \tag{3.25}$$

which defines a relation between $U_2 / U_0 b'$ and kh, displayed in figure 8. The two curves defined by (3.25) separate three regions of existence of the solutions. It can be deduced that for long wavelength (shallow water, $kh \ll 1$), the null solution (fixed point at the origin) is always unstable, while for short waves (deep water, $kh \gg 1$) the null solution is always neutrally stable.

In figure 9(*a*,*b*) we present some time series of the free surface wave. Figure 9(*a*) corresponds to one of the heteroclinic orbits for $\sigma = 2$ connecting s^- to s^+ in the lower half-plane $Y > 0$ of figure 6(*a*). This transition implies a shift by one wavelength of the free surface wave. In figure 9(*b*) the periodic state oscillating around two amplitudes corresponds to the closed orbit just outside the saddle point of figure 6(*b*).

4. Weakly oscillatory current

Pure steadiness in U is an extreme idealization of nature. In reality U is more likely to be a complex function of different time and space scales. We now turn to the main objective of this paper and assume U to be close to the critical value but a slowly oscillating function of time about a steady mean: $U = U(t_2)$ in accordance with (2.11). With this choice the time derivative of U appears at $O(\epsilon^4)$ and the evolution equation remains unchanged in form within the present degree of accuracy. Specifically we let U_2 have a steady part and a sinusoidal part varying with t_2

$$U_2 = \overline{U}_2 + U_2' \cos\omega T, \tag{4.1}$$

where T is the dimensionless time normalized by (3.3) for synchronous resonance and by (3.14) for subharmonic resonance. The dimensionless frequency is ω. The sinusoidal variation in (4.1) is of course a simplification of a transient current in nature which must require many more harmonics for a proper representation.

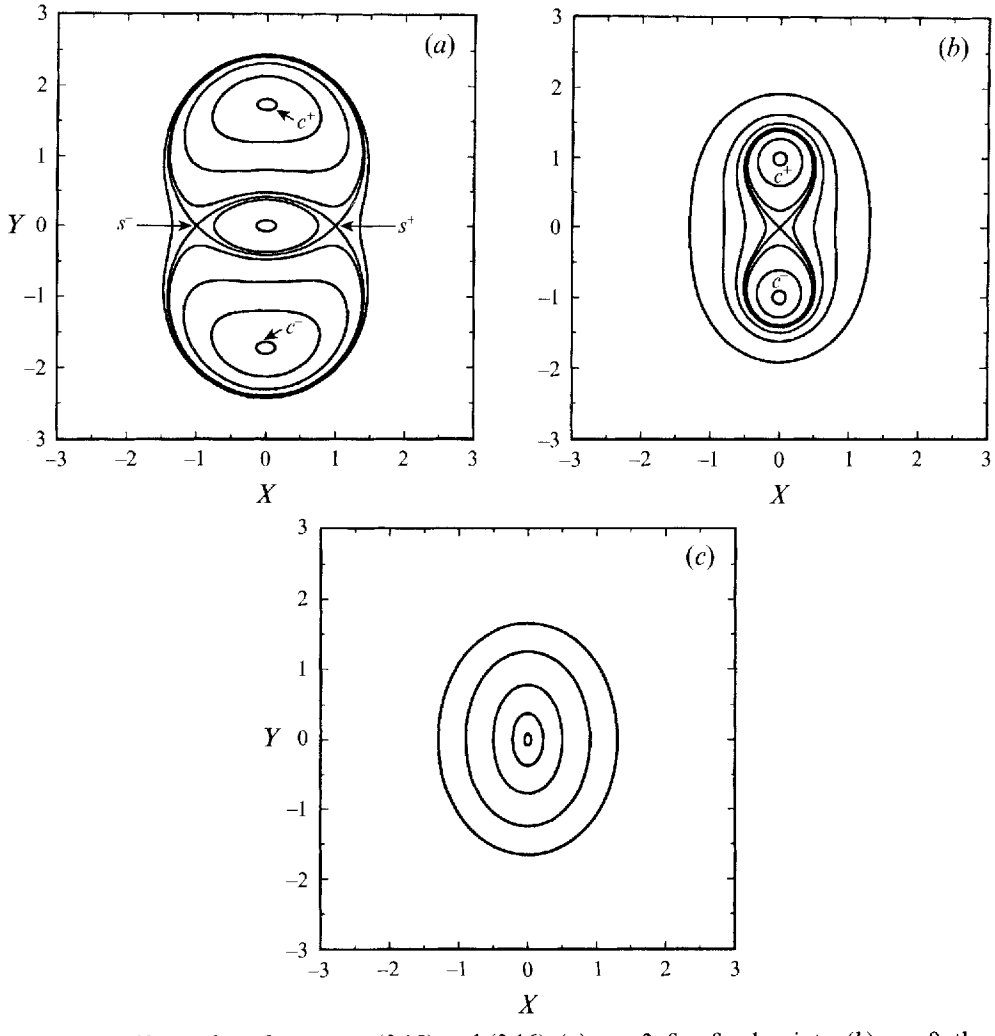

FIGURE 6. Phase plane for system (3.15) and (3.16). (*a*) $\sigma = 2$, five fixed points; (*b*) $\sigma = 0$, three fixed points; (*a*) $\sigma = -1$, one fixed point.

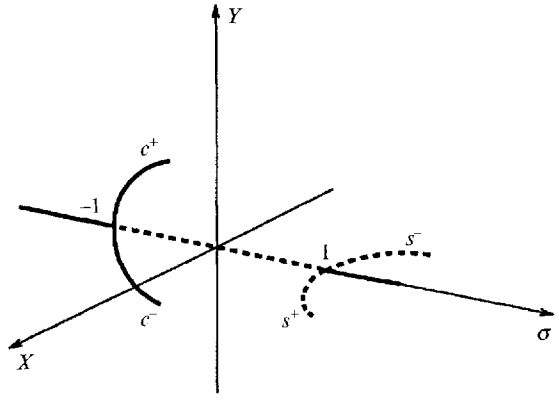

FIGURE 7. Bifurcation diagram for subharmonic resonance.

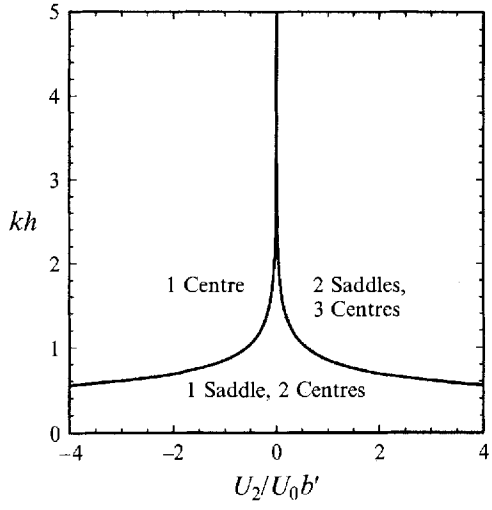

FIGURE 8. Stability diagram for subharmonic resonance. The null solution is always unstable in shallow water, and stable in deep water.

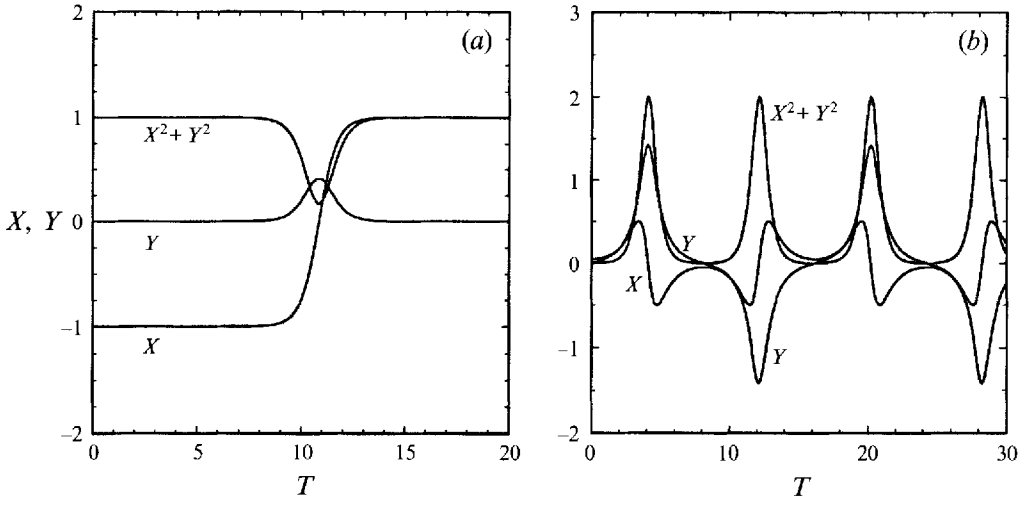

FIGURE 9. Sample time series for different initial phase points and values of σ. (*a*) $X(0) = -0.999$, $Y(0) \approx 0.0001$, on one heteroclinic connection between s^- and s^+ for $\sigma = 2$; (*b*) $X(0) = 0.05$, $Y(0) = 0$, near the origin for $\sigma = 0$.

4.1. *Synchronous resonance*

The system (3.4) and (3.5) is changed to

$$X_T = \sigma Y - (X^2 + Y^2)Y + \mu Y \cos \omega T, \tag{4.2}$$

$$Y_T = -\sigma X + (X^2 + Y^2)X + 1 - \mu X \cos \omega T, \tag{4.3}$$

with σ given by (3.6), and μ given by

$$\mu = \left\{ \frac{b'^2}{4\cosh^2 kh} \left[\frac{2}{\cosh^2 kh} + \frac{3(1 + 2\cosh^2 kh)}{\sinh^4 kh} + 8 \right] \right\}^{-1/3} \frac{U_2'}{U_0},$$

i.e.
$$\frac{\sigma}{\overline{U}_2} = \frac{\mu}{U_2'}. \tag{4.4}$$

Now σ signifies the time-averaged velocity detuning, while the new parameter μ signifies the amplitude of oscillatory detuning. Their dependence on the physical parameters kb and kh are the same. In particular they both increase from zero when $kh = 0$ to a finite limit for $kh \gg 1$. However they become unbounded as $kb \to 0$, and approach zero for $kb \gg 1$.

The dynamical system (4.2), (4.3) is similar to that for a Duffing oscillator with a periodic restoring force and external forcing (Yagasaki *et al.* 1990, eq. (17)). Both systems are obtained through averaging over the fast time scale. The analogous forcing term in the averaged Duffing oscillator originates from the periodic restoring force term, assumed to have a long-period oscillation. By admitting a linear damping term, Yagasaki *et al.* (1990) employed Melnikov's method to estimate the transition to global chaos through homoclinic tangles for initial conditions close to a saddle; the threshold however depends critically on the damping term. In the present problem, damping due to turbulence is far too complex to be satisfactorily modelled at present; only the frictionless system is considered here.

Note first that by the transformation

$$\theta = \omega T, \quad X' = \frac{X}{\omega^{1/2}}, \quad Y' = \frac{Y}{\omega^{1/2}}, \tag{4.5}$$

the dynamical system becomes

$$X'_\theta = \sigma' Y' - (X'^2 + Y'^2)Y' + \mu' Y' \cos\theta, \tag{4.6}$$

$$Y'_\theta = -\sigma' X' + (X'^2 + Y'^2)X' + \frac{1}{\omega\omega^{1/2}} - \mu' X' \cos\theta, \tag{4.7}$$

where

$$\sigma' = \frac{\sigma}{\omega}, \quad \mu' = \frac{\mu}{\omega}. \tag{4.8}$$

In the transformed system (4.6), (4.7) the effect of varying ω is to change the amplitudes σ' and μ' and the abscissa of the fixed points of the autonomous limit, but not their qualitative variety. Therefore we shall take $\omega = 1$ in all subsequent examples; this implies a definite value of the dimensional frequency ω^* for given values of U_0, kh, k, b according to (3.3) and (3.14). With this choice all dimensionless frequencies to be referred to later are frequency ratios relative to the frequency of current oscillation.

We now discuss numerical experiments for the transient response of the non-autonomous system (4.2) and (4.3), for various amplitude of μ and σ, as well as the initial states. The equations are integrated by a fourth-order Runge–Kutta scheme with adaptive stepsize control. Poincaré sections are obtained by sampling the trajectories at the time interval of 2π, the normalized period of the current oscillation, and by projection of the intersection points on the (X, Y)-plane. Each section is obtained by giving a finite number of initial conditions and integrating for a time $T = 2\pi N$, with N varying from 1000 to 2000. The entire phase plane is explored by giving a large number of initial phase points on the X-axis, with a very small increment (~ 0.001) to reveal all the relevant structures. The evolution of the regular curves and the growth of the stochastic layers is then followed. In the unforced case $\mu = 0$, each closed trajectory is characterized by a natural frequency Ω around the centre. The closer the trajectory to the homoclinic loop, the lower the natural frequency (=0 for the loop itself). The highest frequency, given by (3.10), is achieved in a small neighbourhood

of the centre itself. Whenever $\Omega = m/n$ is a rational number different from unity, the Poincaré section of the unforced trajectory appears as a sequence of n points. The current oscillation excites temporal resonances at the m/n ultrasubharmonic frequency. On the other hand, if Ω is an irrational number, the Poincaré section of the trajectory is a closed continuous curve, and if Ω is far enough from a rational number, the closed curve will be preserved for small $\mu > 0$ (KAM theorem).

The most likely temporal resonances in a neighbourhood of the elliptic point of the unperturbed map can be forecast by a naive perturbation analysis. Let $\mu = \nu\mu_1 = O(\nu)$ with $\nu \ll 1$ being an ordering parameter. Expanding around a centre $(X_*, 0)$

$$X = X_* + \nu X_1 + \nu^2 X_2 + \nu^3 X_3 + \ldots,$$
$$Y = \quad \nu Y_1 + \nu^2 Y_2 + \nu^3 Y_3 + \ldots,$$

we get from (4.2) and (4.3) at $O(\nu)$:

$$X_{1_T} - \frac{1}{X_*} Y_1 = 0,$$
$$Y_{1_T} - \left(3X_*^2 - \sigma\right) X_1 = -\mu_1 X_* \cos T,$$

which is a forced harmonic oscillator with the natural frequency given by (3.10). The first-order solution is therefore

$$X_1 = X_{11}^n e^{i\Omega T} + X_{11}^f e^{iT} + *, \qquad Y_1 = Y_{11}^n e^{i\Omega T} + Y_{11}^f e^{iT} + *,$$

where the superscript n denotes natural mode response, and f the forced response. Clearly resonance occurs if $\Omega = \pm 1$. At the second order $O(\nu^2)$, the perturbation equations are

$$X_{2_T} - \frac{1}{X_*} Y_2 = -2X_* X_1 Y_1 + \mu_1 Y_1 \cos T,$$
$$Y_{2_T} - \left(3X_*^2 - \sigma\right) X_2 = 3X_* X_1^2 + X_* Y_1^2 - \mu_1 X_1 \cos T,$$

which is again a harmonic oscillator of natural frequency Ω forced at the frequencies $\pm 2\Omega, \pm(\Omega \pm 1), \pm 2, 0$. Hence the second-order solution is of the form

$$X_2 = X_{21}^n e^{i\Omega T} + X_{20}^f + X_{21}^f e^{i(\Omega-1)T} + X_{22}^f e^{i2\Omega T} + X_{23}^f e^{i(\Omega+1)T} + X_{24}^f e^{i2T} + *,$$
$$Y_2 = Y_{21}^n e^{i\Omega T} + Y_{20}^f + Y_{21}^f e^{i(\Omega-1)T} + Y_{22}^f e^{i2\Omega T} + Y_{23}^f e^{i(\Omega+1)T} + Y_{24}^f e^{i2T} + *.$$

At this order resonances occur when any of the forcing frequencies are equal to $\pm\Omega$, i.e. when $\Omega = 1/2, 2$. At the third order $O(\nu^3)$

$$X_{3_T} - \frac{1}{X_*} Y_3 = -\left[2X_*\left(X_2 Y_1 + X_1 Y_2\right) + Y_1^3 + Y_1 X_1^2\right] + \mu_1 Y_2 \cos T - X_{1_{T_2}},$$
$$Y_{3_T} - \left(3X_*^2 - \sigma\right) X_3 = 6X_* X_1 X_2 + 2X_* Y_1 Y_2 + X_1^3 + X_1 Y_1^2 - \mu_1 X_2 \cos T - Y_{1_{T_2}},$$

the quadratic and cubic terms on the right force oscillations at the natural frequency $\pm\Omega$ and at the following frequencies: $\pm 2\Omega, \pm 3\Omega, \pm(\Omega \pm 2), \pm(2\Omega \pm 1), \pm 3, \pm 1$. At this order resonances occur if $\Omega = 1/3, 1/2, 2$ and 3. Other ratios can be relevant if the perturbation analysis is carried to higher order, implying longer time for resonant growth. As usual, the secular terms can be eliminated by a multiple-scale analysis for uniform validity in time. While this is not pursued here, the recognition of these temporal resonances facilitates the understanding of the numerical results to be discussed next. Note that the frequency ratios for these temporal resonances

estimated by a third-order analysis are the same as the wavelength ratio of the spatial resonances due to the waviness of the bed.

Note that the system (4.3) and (4.4) has a time-varying Hamiltonian,

$$H(X, Y, T) = \tfrac{1}{2}\sigma(X^2 + Y^2) - \tfrac{1}{4}(X^2 + Y^2)^2 - X + \tfrac{1}{2}\mu(X^2 + Y^2)\cos T. \tag{4.9}$$

According to the theory of Hamiltonian systems, one should expect regions of stochasticity in the Poincaré section confined by invariant KAM curves; the latter are curves on which, in the unforced integrable case, the frequency ratio is 'sufficiently' irrational to allow the curve to be preserved for small perturbation from integrability. In particular, as μ increases from 0, regions of stochasticity first appear near the hyperbolic fixed points of the unperturbed (i.e. $\mu = 0$) Poincaré map; their size also increases so that finally neighbouring KAM curves are destroyed. It is known that these regions are generated by transversal intersections (homoclinic tangle) of the stable and unstable manifolds of the above hyperbolic fixed points. There are other regions of stochasticity which arise for increasing μ. According to the Poincaré–Birkhoff theorem (Lichtenberg & Liebermann 1992, p. 183), if a closed curve surrounding an elliptic fixed point has a rational rotation number, say, m/n, at least two n cycles of alternating n hyperbolic and n elliptic fixed points are expected to develop when $\mu > 0$. To the present accuracy, transversal intersection of the manifolds of the n hyperbolic points generates stochastic layers which surround the islands of regular motion around each of the n elliptic points (which form an n-island chain). When μ increases from zero, the first regions of stochasticity to appear are those for low values of n. The cycles for large n are of very small extent, therefore difficult to detect. More complexity is added to the picture if we consider the nth Poincaré map, obtained by sampling the trajectories after every time interval of $2\pi n$. A point of the nth elliptic cycle becomes an elliptic fixed point of the latter map, therefore all of the above structure repeats itself around it: stochastic layers surrounding island chains confined by regular KAM curves. This hierarchical structure repeats itself indefinitely. For small μ each island chain and associated stochastic layer are confined between KAM curves. Transition to global stochasticity occurs for values of μ such that neighbouring stochastic layers overlap and destroy the separating KAM curves. It is of interest to find the value of μ beyond which the Poincaré map has no more fixed points, and the whole Poincaré section is fully stochastic (complete stochasticity). We now examine numerically the development of these events.

We first fix the value of σ to 2.5 and increase μ from 0. The Poincaré map of the autonomous system has two elliptic and one hyperbolic fixed points (whose nature and coordinate are the same as c_1, c_2 and s of figure 2*a*). By Melnikov's method one can show that the condition for the onset of homoclinic tangle is simply $\mu > 0$, since there is no damping. Therefore a stochastic layer first appears in the $O(\mu)$ neighbourhhood of the hyperbolic fixed point of the Poincaré map. This can be seen in figure 10(*a*) computed for $\mu = 0.01$. The stochastic layer is confined between three KAM curves which surround the two elliptic points of the map. Most of the trajectories are still regular, i.e. they lie on a torus. To the left and to the right of the smaller loop of the tangle, two new islands can be seen. The island on the left, I_l, is clearly visible, while the island on the right, I_r, is 'compressed' between adjacent invariant curves (not shown for clarity); corresponding to each of the new islands there is one hyperbolic point. I_l is a synchronous resonance $\Omega = 1$, while I_r is an ultraharmonic resonance $\Omega = 2$, as was verified by taking a Poincaré section sampled at time intervals equal to π instead of 2π in which I_l then appears as a

two-island chain, while I_r remains unchanged. This can be further understood if we note (from (3.10)) that for $\sigma = 2.5$ the linearized frequency of oscillation around c_2 of figure 2(*a*) is $\Omega = 2.1$. Because the frequency of the homoclinic loop is zero, between the centre and the homoclinic orbit there must be an orbits with angular frequencies $\Omega = 2, 1, 1/2, 1/3$, etc., which are subject to resonance when forced at $\omega = 1$. Clearly, among these the frequency $\Omega = 2$ is the closest to $\Omega = 2.1$ at which island chains are expected to emerge, according to the Poincaré–Birkhoff theorem. The frequencies $1/2$ and $1/3$ are close enough to that of the homoclinic orbit, so that homoclinic tangles quickly create stochastic layers to overwhelm details at the threshold of resonance. On the other hand, the linearized frequency of oscillation around c_1 of figure 2(*a*) is $\Omega = 1.95$, hence a one-island chain must be the result of $\Omega = 1$ resonance. It is around I_l that a hierarchy of higher-order islands and stochastic layers will emerge when μ further increases. At $\mu = 0.02$ the size of the stochastic region thickens, as seen in figure 10(*b*). There is now a richer structure with secondary resonances around this primary island. Secondary island chains with associated stochastic layers are revealed by a magnification of the section as shown in figure 10(*c*). As a whole, the region of stochasticity is still a small fraction of the region occupied by regular curves (figure 10*b*). The growth of the stochastic layers continues as μ is increased. When $\mu = 0.1$ the region of stochasticity has grown considerably at the expense of I_l, as shown in figure 10(*d*). As the parameter μ increases further, the stochastic sea further expands. Figure 10(*e*) shows the Poincaré section for $\mu = 0.5$. The stochastic region has swallowed the two regular regions of figure 10(*d*) and encloses the crescent-like region of regular motion. Transition to global stochasticity is approaching. The disappearance of the crescent-like region of regular motion, with the destruction of its last KAM curve, happens for values of $\mu \approx 2.3$. Any initial conditions inside the stochastic region give rise to successive intersections which wander in the stochastic region, getting arbitrarily close to any given point (the trajectories are dense). A Poincaré section for $\mu = 2.25$ is shown in figure 10(*f*). The region of stochasticity is now circular and dense, and is bounded by an external KAM curve. The remnant of the above crescent-like region is a tiny island around $X \sim -2.65, Y \sim 0$ which disappears for $\mu > 2.3$.

The transition to chaos can be alternatively displayed via the power spectra of a trajectory. For several different initial conditions we have examined the spectral evolution for given σ and increasing values of μ. As an example let us consider the initial condition with $(X(0), Y(0)) = (0.4, 0)$ which is very close to c_2, and for $\sigma = 2.5$. For $\mu = 0.01$, figure 11(*a*) shows that the dominant frequency is the natural $\Omega = 2.1$, in agreement with the perturbation analysis. Note the spectral peaks not only at the forcing frequency $\omega = 1$, but also at $\Omega \pm 1$ and 2Ω. For larger values of μ, an increasing number of harmonics appears in the spectrum. In figure 11(*b*) for $\mu = 0.1$, we observe peaks at $\Omega \pm 2$, 2 and 3. From this state of quasi-periodicity, transition to chaos occurs for larger values of μ. At $\mu = 0.5$, the spectrum of figure 11(*c*) is broad-banded implying chaos. Referring to figure 10, we see that for $\mu = 0.01$ and 0.1 the chosen initial conditions fall in the region of regular motion (see figure 10*a*,*d*), while for $\mu = 0.5$ they fall in the stochastic layer (see figure 10*e*). This pattern of evolution is typical. Indeed, for any σ and μ, if the initial phase point lies outside the stochastic layer, the corresponding spectrum is composed of lines (natural, forcing and their interacting harmonics) as in figure 11(*a*,*b*); on the other hand, if the initial phase point lies in the stochastic layer, the spectrum is similar to figure 11(*c*). In the following we shall only discuss our results by using the Poincaré map.

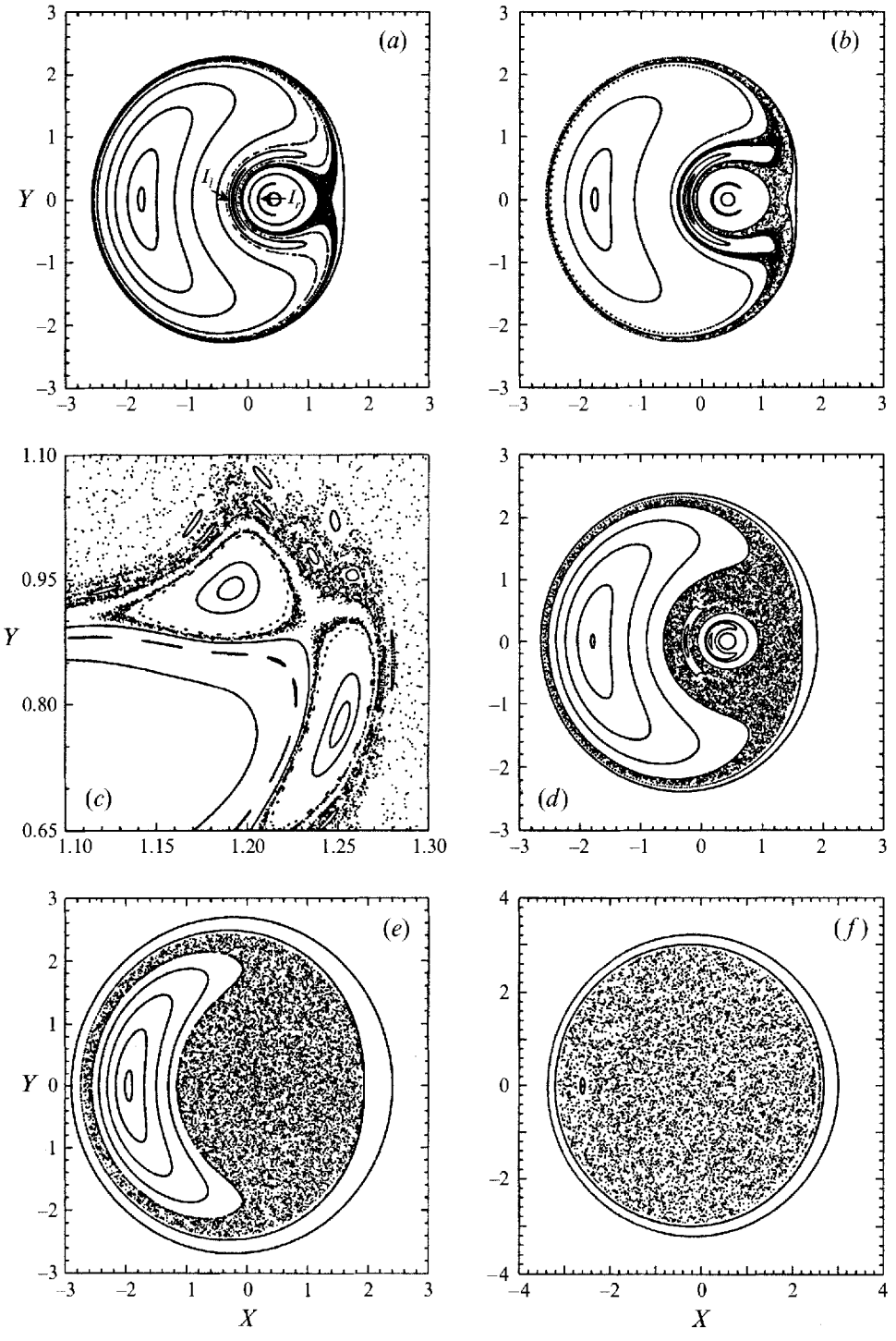

FIGURE 10. Poincaré sections for $\sigma = 2.5$ and increasing values of μ. (*a*) $\mu = 0.01$; (*b*) $\mu = 0.02$; (*c*) $\mu = 0.02$, magnification of secondary islands; (*d*) $\mu = 0.1$; (*e*) $\mu = 0.5$; (*f*) $\mu = 2.25$.

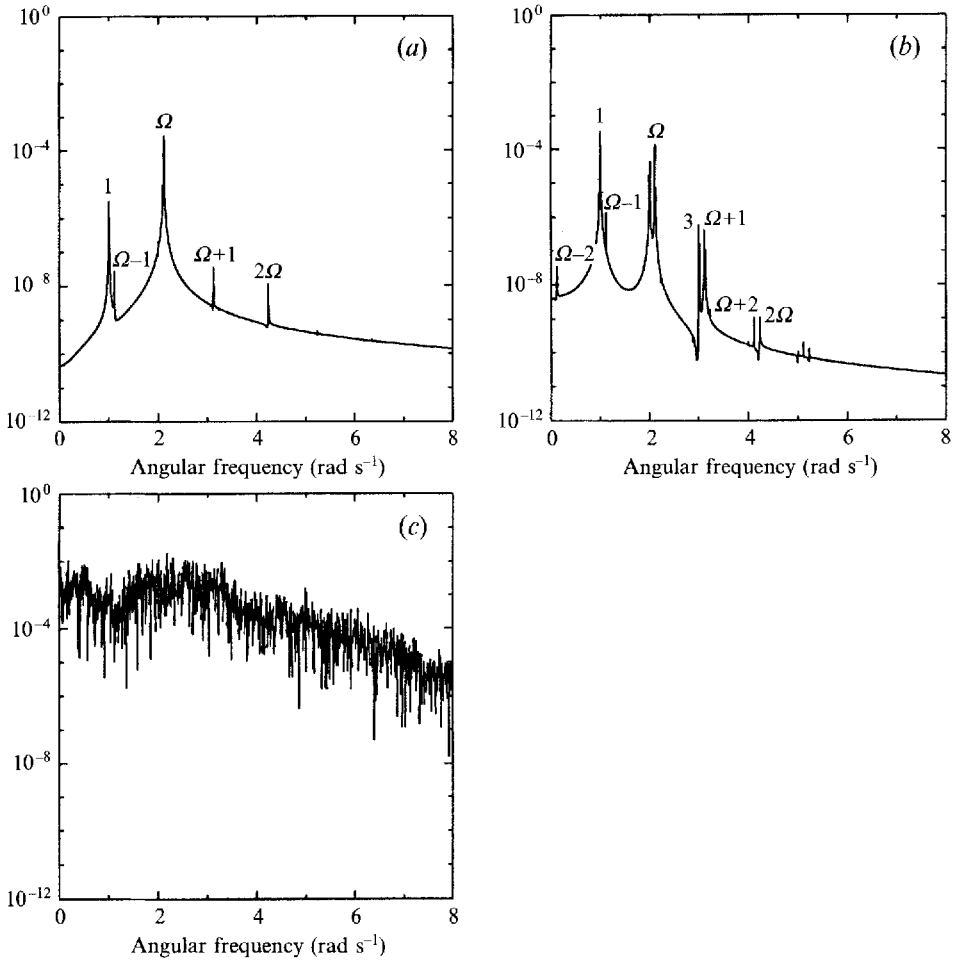

FIGURE 11. Power spectra for fixed initial condition $(X(0), Y(0)) = (0.4, 0)$ and increasing values of μ. (*a*) $\mu = 0.01$; (*b*) $\mu = 0.1$; (*c*) $\mu = 0.5$.

We now consider $\sigma < 3/4^{1/3}$, for which the autonomous system has only one elliptic fixed point (c_1 in figure 2*c*). For $\mu > 0$ the elliptic point of the Poincaré map is at a distance $O(\mu)$ from the original centre for zero oscillatory current. Having no hyperbolic fixed points for $\mu = 0$, there is no homoclinic tangle for very small μ. Only for larger values of μ can stochastic layers appear. Below, we follow the development for $\sigma = -1$ and increasing values of μ. In figure 12(*a*) the Poincaré section for $\mu = 0.1$ is shown. One elliptic and one hyperbolic point are born in an anulus between two KAM curves. The new elliptic point c_3 is an ultraharmonic $\Omega = 2$ resonance, which can be expected since for this σ (and $\mu = 0$) the linearized frequency of oscillation around c_1 is $\Omega = 1.8742$, according to (3.10), and the frequency of large orbits is greater. The map has now two elliptic points and one hyperbolic point; no stochastic layers have yet developed. As μ increases to 0.3 (figure 12*b*) the island around c_3 becomes larger and is squeezed against neighbouring KAM curves. For $\mu \approx 0.4$ the manifolds of the hyperbolic point s tangle and give rise to a stochastic layer, shown in figure 12(*c*) for $\mu = 0.5$. Now the whole section strongly resembles figure 10(*b*,*e*) for $\sigma > 3/4^{1/3}$. If we further increase μ the Poincaré section becomes more complex.

In figure 12(*d*) for $\mu = 0.7$ the region of regular motion is still crescent-like. The elliptic point and associated region of regular motion encircled by the stochastic layer for $\mu = 0.5$ (seen in figure 12*c*) have now disappeared. The magnified structure of the island chains is shown in figure 12(*e*); second-order island chains and associated stochastic layers are seen around each point of the first-order chains. These primary island chains are all ultrasubharmonic temporal resonances, since $\Omega > 1$ everywhere in the section. The disappearance of the crescent-like region of regular motion takes place at $\mu \approx 1.39$. Note that the final form of the stochastic layer is independent of the value of σ, i.e. of the number and nature of the fixed points of the unperturbed Poincaré map.

Comparing the two cases with $\sigma \gtrless 3/4^{1/3}$, we see that for smaller $|\sigma|$, chaos begins at a larger μ. For further confirmation, we have performed a computation for $\sigma = 0$; indeed the start of local chaos, still triggered by the tangle of the manifolds of the $\Omega = 2$ resonance, occurs at the intermediate value of $\mu \approx 0.29$.

4.2. *1/2 subharmonic resonance*

The system (3.15), (3.16) is changed to

$$X_T = (1+\sigma)Y - (X^2+Y^2)Y + \mu Y \cos\omega T, \tag{4.10}$$

$$Y_T = (1-\sigma)X + (X^2+Y^2)X - \mu X \cos\omega T, \tag{4.11}$$

with σ still given by (3.14) but μ by

$$\mu = \left\{ b' \left[\sinh 2kh + \frac{1}{2\sinh 2kh} + \frac{1}{4}(1 - 2\sinh^2 kh)(\tanh kh + \frac{3}{\tanh^2 kh}) \right] \right\}^{-1} \frac{U_2'}{U_0}, \tag{4.12}$$

i.e. $\sigma/\overline{U}_2 = \mu/U_2'$. Note again that both σ and μ have the same dependence on the physical parameters kb and kh. In particular both are decreasing functions of kb and increasing functions of kh. As kh increases from 0 to infinity, σ and μ rise from 0 to finite limits. For small kb, σ and μ are unbounded but approach finite limits for $kb \gg 1$.

By the same transformation of variables (4.5) and the same redefinition of parameters (4.8), the preceding system can be rewritten as

$$X_\theta' = (\frac{1}{\omega\omega^{1/2}} + \sigma')Y' - (X'^2 + Y'^2)Y' + \mu' Y' \cos\theta, \tag{4.13}$$

$$Y_\theta' = (\frac{1}{\omega\omega^{1/2}} - \sigma')X' + (X'^2 + Y'^2)X' - \mu' X' \cos\theta. \tag{4.14}$$

Again the effect of ω is to change the location of the fixed points of the autonomous system, without changing the variety. Below, we shall take $\omega = 1$ as being representative.

For $\mu > 0$, the system (4.10), (4.11) possesses a time-dependent Hamiltonian:

$$H(X,Y,T) = \frac{1}{2}\sigma(X^2+Y^2) - \tfrac{1}{4}(X^2+Y^2)^2 + \frac{1}{2}\sigma(Y^2-X^2) + \frac{1}{2}\mu(X^2+Y^2)\cos T \tag{4.15}$$

and is no longer integrable.

Recall that in the autonomous limit, the unforced system has one centre if $\sigma < -1$, two if $-1 < \sigma < 1$ and three if $\sigma > 1$. We now follow the transition to global stochasticity for three values of σ and increasing μ. For reference we have used the naive perturbation analysis similar to that in §4.1, and shown that around the origin where the natural frequency of a small closed orbit is given by (3.21), temporal

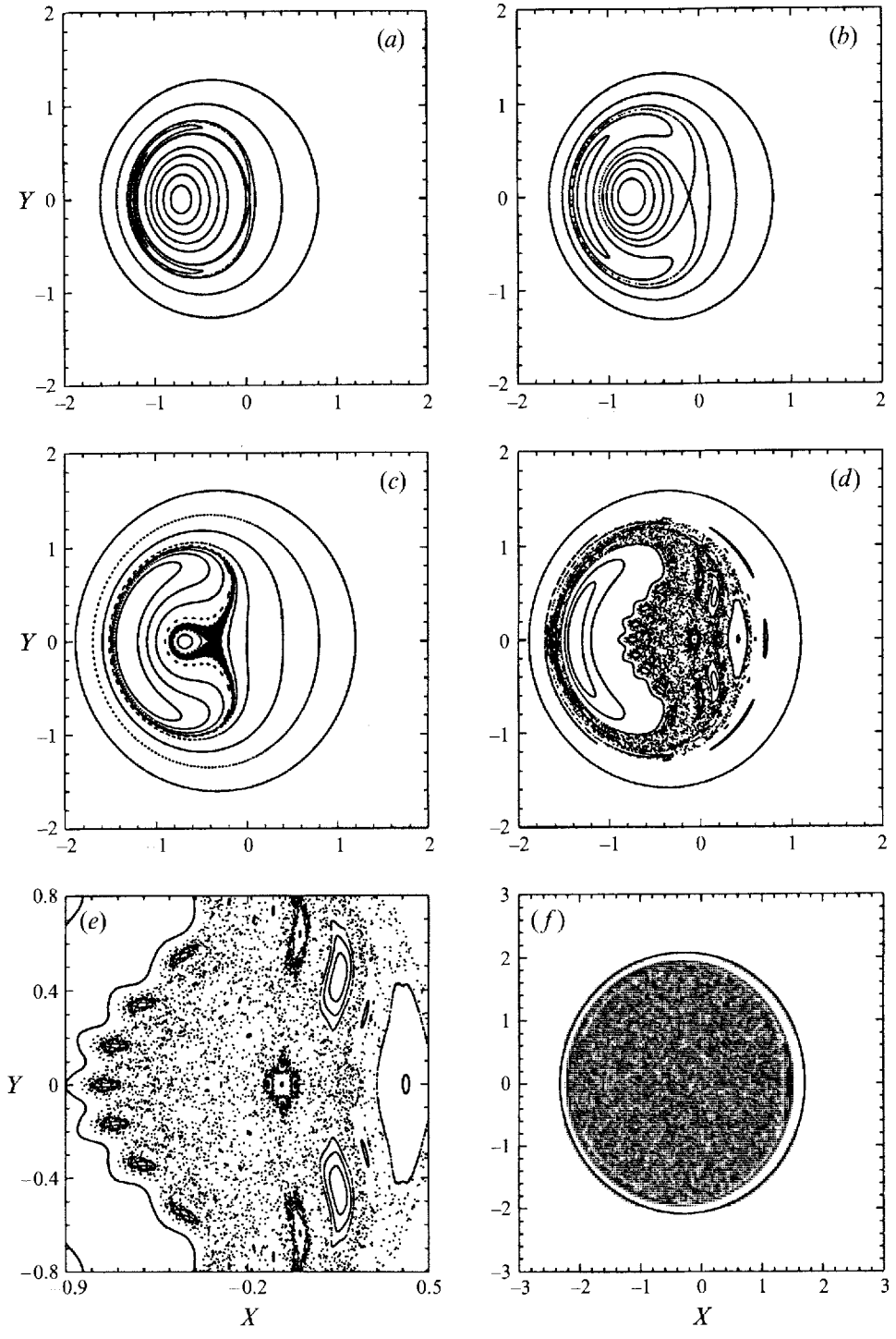

FIGURE 12. Poincaré sections for $\sigma = -1.0$ and increasing values of μ. (*a*) $\mu = 0.1$; (*b*) $\mu = 0.3$; (*c*) $\mu = 0.5$; (*d*) $\mu = 0.7$; (*e*) $\mu = 0.7$, magnification showing secondary islands; (*f*) $\mu = 1.7$.

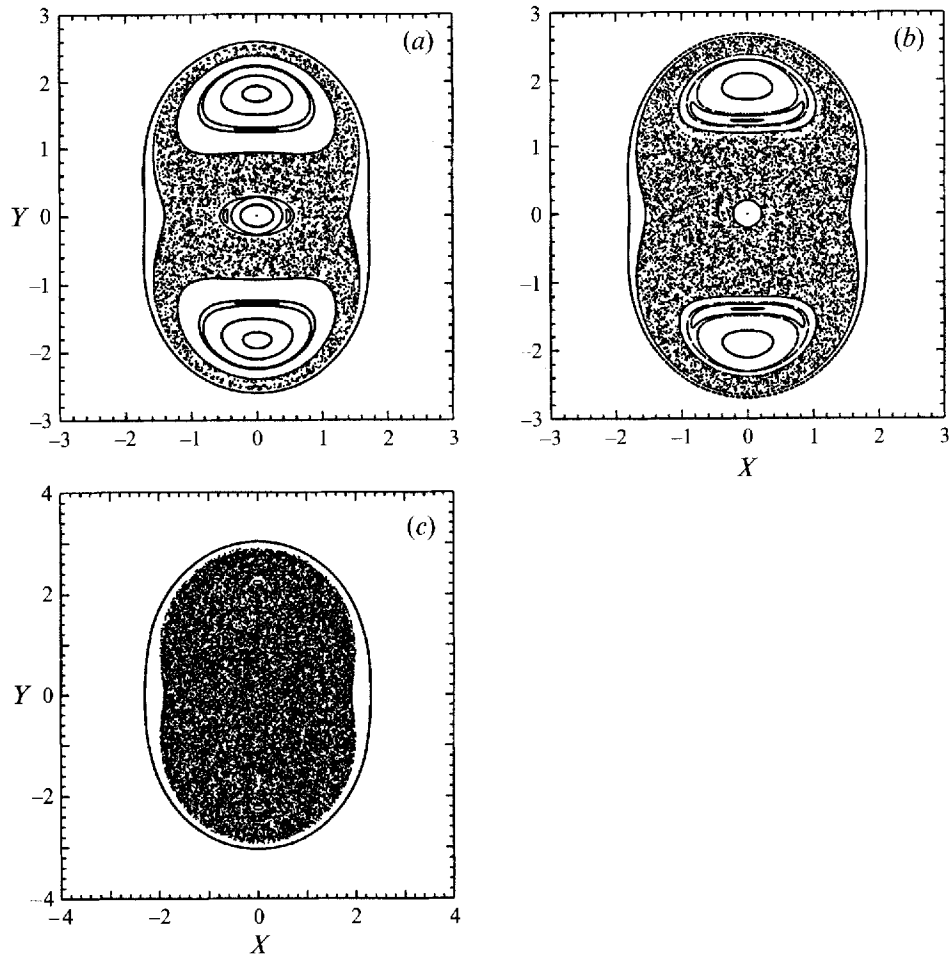

FIGURE 13. Poincaré sections for $\sigma = 2.0$ and increasing values of μ. (*a*) $\mu = 0.3$; (*b*) $\mu = 0.6$; (*c*) $\mu = 1.5$.

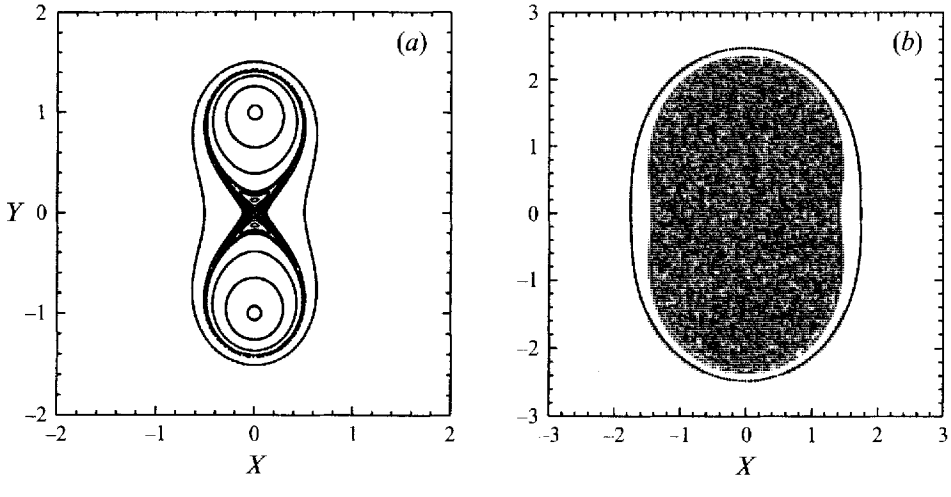

FIGURE 14. Poincaré sections for $\sigma = 0$ and increasing values of μ. (*a*) $\mu = 0.003$; (*b*) $\mu = 1.5$.

resonance does not occur at $O(v)$; instead it happens at $O(v^2)$ if $\Omega = 1/2$, and at $O(v^3)$ if $\Omega = 1, 1/3$. On the other hand around a centre on the y-axis where the natural frequency of a small closed orbit is given by (3.23), temporal resonances can be forced at $O(v)$ if $\Omega = 1$, at $O(v^2)$ if $\Omega = 1/2, 2$ and at $O(v^3)$ if $\Omega = 1/3, 3$

We first consider $\sigma = 2$. In this case the natural frequency around the origin is $\Omega = 1.73$, according to (3.21). Corresponding to the other two centres on the Y-axis, we find $\Omega = 3.46$, according to (3.23). For $\mu = 0.3$ the section of figure 13(a) shows a two-island chain around the origin, which is the result of an $\Omega = 1/2$ resonance appearing first (at $O(v^2)$) according to the perturbation theory. The expected $\Omega = 1$ resonance at $O(v^3)$ is obliterated by the rapid growth of the stochastic layer. Around the other two centres on the Y-axis two one-island chains are developed as a result of an $\Omega = 3$ resonance; the other one-island chains ($\Omega = 1$ and $\Omega = 2$ resonance) are swallowed in the stochastic layer for smaller values of μ. When $\mu = 0.6$ the islands corresponding to the $\Omega = 2$ resonances have grown considerably in size. They are shown in figure 13(b), together with the corresponding hyperbolic points, which are about to tangle. At large enough μ the regular region around the centre at the origin disappears. Figure 13(c) shows the Poincaré section for $\mu = 1.5$ where the regions of regular motion have reduced to two tiny islands, which disappear for $\mu = 1.6$.

When $\sigma = 0$ (no steady detuning, i.e. the detuning is purely oscillatory) the unperturbed system has two elliptic and one hyperbolic fixed points. Around the two elliptic points the natural frequency is $\Omega = 2$, hence resonance occurs in a neighbourhood of these points. We also expect to detect an $\Omega = 1$ resonance. In figure 14(a) the Poincaré section for $\mu = 0.003$ is shown. The motion is mostly regular, except for the eight-shaped stochastic layer originated by the tangle of the manifolds of the hyperbolic point. In the picture the two synchronous $\Omega = 1$ resonances are visible near the origin. Figure 14(b) shows the section for $\mu = 1.5$, when there are no more islands and the motion is completely stochastic.

Finally we consider $\sigma = -2$ for which the unforced system has only one elliptic fixed point at the orgin. Again, the natural frequency increases as we leave the origin. According to (3.21), the linearized frequency about the origin is $\Omega = 1.73$, implying that when $\mu > 0$ the first chain to be detected will be the one originated from the trajectory with $\Omega = 2$. Indeed two elliptic, c^+ and c^-, and two hyperbolic, s^+ and s^-, fixed points are born, and they are compressed between two KAM curves in figure 15(a) for $\mu = 0.5$. No stochastic layers have developed as yet. Note that the two new elliptic points do not constitute a two-island chain. If the initial condition is given around one of the elliptic point, successive intersections remain in its own basin, describing either a regular curve or a secondary island chain. Figure 15(b) shows a sample section for $\mu = 0.7$. The regions of stochasticity are still undetectable, but the two regions around c^+ and c^- have grown in size. For a larger μ ($\mu = 0.9$) the section reveals all the complex structure developed by the tangle of the manifolds of s^+ and s^-, resembling the results for $\sigma > 1$, and showing the island chains evolving near the borders of the regular regions (figure 15c). Increasing the valuc of μ causes transition to total stochasticity. The three regions of regular motion gradually reduce in size but new island chains are developed at every boundary between regular and stochastic regions. Particularly complex are the Venetian mask-like regions in figure 15(d) for $\mu = 1.1$. In figure 15(e) the section is magnified to reveal the secondary four-island chain around c^+ and the stochastic layer generated by the tangles from the four hyperbolic points. Further, tertiary six-island chains are around each of the four elliptic points. Figure 15(f) shows the section for

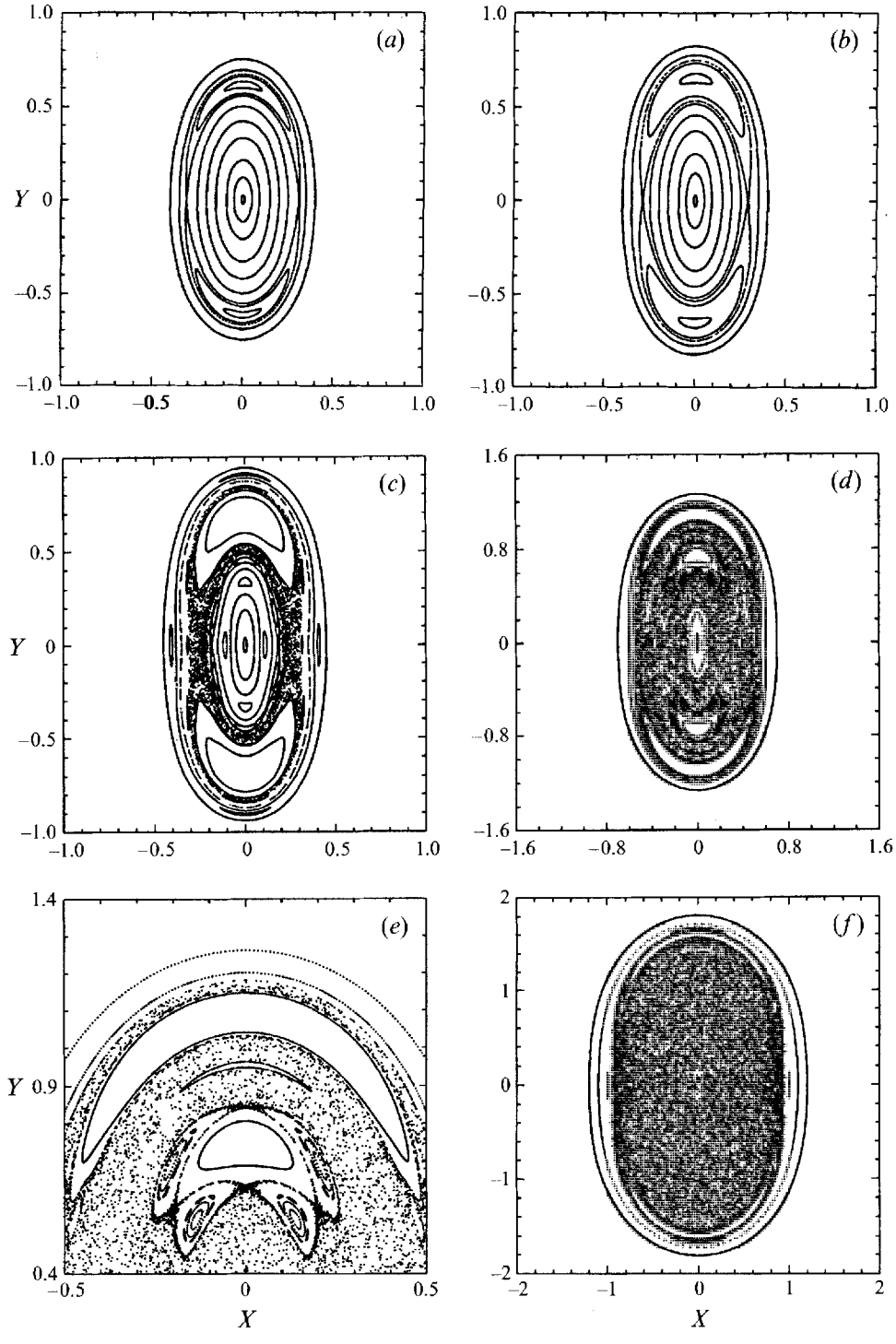

FIGURE 15. Poincaré sections for $\sigma = -2.0$ and increasing values of μ. (*a*) $\mu = 0.5$; (*b*) $\mu = 0.7$; (*c*) $\mu = 0.9$; (*d*) $\mu = 1.1$; (*e*) $\mu = 1.1$, magnification showing secondary and tertiary islands; (*f*) $\mu = 1.7$.

$\mu = 1.7$: the internal regions of regular motion have disappeared, and two small islands still remain near the outer KAM curve. Note that the final stochastic state is almost the same as that for $\sigma = 2$. The difference is that for $\sigma < -1$, i.e. for lower mean speed of the current, the number of hyperbolic points in the original unforced system is zero; tangling of manifolds begins at larger μ after hyperbolic points are formed.

5. Concluding remarks

In this paper we have studied the effect of nonlinearity on the free surface wave resonated by a steady or nearly steady current over a wavy bed. Resonance of surface waves of a given length is shown to be possible over bed waves with synchronous, subharmonic, or ultraharmonic wavelengths. The instability of the nonlinear wave on the free surface is studied by deducing the evolution equations without viscosity. When the current is strictly steady, the possible nonlinear steady states and their stability are studied as a function of the velocity detuning parameter σ. Triggered by instability, different transient but regular nonlinear states are found for different ranges of σ.

We have further examined the effect of a time-harmonic perturbation in the resonating current. The qualitative consequence is shown to be dramatically different from the strictly steady case because the non-integrable Hamiltonian system may yield chaos in the manner predicted qualitatively by KAM and the Poincaré–Birkhoff theorem. The dependence on the strength of the oscillatory current, represented by the parameter μ, for several typical values of σ representing different regimes of steady detuning have been studied numerically in detail. Bifurcation thresholds are identified with both synchronous and superharmonic resonances, by numerical and analytical means through a simple perturbation analysis. While sufficiently large μ always leads to global stochasticity, there are similarities as well as differences in the details of transition to chaos. If the current involves more harmonics the chaotic response must be more complex.

As cited in the Introduction, the problem of waves induced by a current over wavy boundaries is of broad interest. Thus far all existing studies have been for inviscid fluids. On the same basis we have examined the consequence of unsteadiness in the current. Of course many factors existing in nature can further complicate the physics. For instance, qualitative as well as quantitative changes can be expected when dissipation is considered in the flow. For this purpose the primary flow must be sheared, and turbulence must be accounted for over the wavy bed. Of possible interest is the flow over a large but finite number of dunes in a river affected by weak tides. The slow spatial variation of the bed amplitude must affect the free surface wave, whose space–time evolution must then be studied by the nonlinear cubic Schrödinger equation derived in § 2. For a current with a small oscillatory component the Schrödinger equation must have slowly time-varying harmonic coefficients; spatial and temporal chaos must occur as shown in a similar study by Naciri & Mei (1992)

This research was supported by Office of Naval Research through the Accelerated Research Initiative on Nonlienar Ocean Waves (Contract N00014-92-J-1754) and by the US National Science Foundation (Grant CTS 9115689). P. Sammarco also acknowledges the support of a fellowship from the University of Naples '*Federico II*'. Comments by Professor Oded Gottlieb at the initial stage of this study have been helpful.

REFERENCES

BONTOZOGLOU, V., KALLIADASIS, S. & KARABELAS, A. J. 1991 Inviscid free surface flow over a periodic wall. *J. Fluid Mech.* **226**, 189–203.

HALL, P. & SEMINARA, G. 1980 Nonlinear oscillations of non-spherical cavitation bubbles in acoustic fields. *J. Fluid Mech.* **101**, 423-444.

JORDAN, D. W. & SMITH, P. 1986 *Nonlinear Ordinary Differential Equations.* Clarendon Press.

KENNEDY, J. F. 1963 The mechanics of dunes and antidunes in erodible-bed channels. *J. Fluid Mech.* **16**, 521–544.

LAMB, H. 1932 *Hydrodynamics.* Dover.

LICHTENBERG, A. J. & LIEBERMANN, M. A. 1992 Regular and Chaotic Dynamics. Springer.

MEI, C. C. 1969 Steady free surface flow over a wavy bed. *J. Engng Mech. Div. ASCE* EM **6**, 1393–1402.

MEI, C. C. 1989 *The Applied Dynamics of Ocean Surface Waves.* World Scientific.

MILES, J. W. 1986 Weakly nonlinear Kelvin–Helmholtz waves. *J. Fluid Mech.* **172**, 513–529.

NACIRI, M. & MEI, C. C. 1992 Evolution of a short surface wave on a very long surface wave of finite amplitude *J. Fluid Mech.* **235**, 415–452.

YAGASAKI, K., SAKATA, M. & KIMURA, K. 1990 Dynamics of a weakly nonlinear system subjected to combined parametric and external excitation. *Trans. ASME* E: *J. Appl. Mech.* **57**, 209–217.

ZHU, S. 1992 Stationary Binnie waves near resonance. *Q. Appl. Maths* **50**, 585–597.